

REACTION KINETICS OF MUONIUM WITH
HYDROGEN BROMIDE

By

Alexandra Tempelmann

B. Sc. (Chemistry) University of Waterloo

A THESIS SUBMITTED IN PARTIAL FULFILLMENT OF
THE REQUIREMENTS FOR THE DEGREE OF
MASTER OF SCIENCE

in

THE FACULTY OF GRADUATE STUDIES
CHEMISTRY

We accept this thesis as conforming
to the required standard

THE UNIVERSITY OF BRITISH COLUMBIA

November 1990

© Alexandra Tempelmann, 1990

In presenting this thesis in partial fulfilment of the requirements for an advanced degree at the University of British Columbia, I agree that the Library shall make it freely available for reference and study. I further agree that permission for extensive copying of this thesis for scholarly purposes may be granted by the head of my department or by his or her representatives. It is understood that copying or publication of this thesis for financial gain shall not be allowed without my written permission.

Department of Chemistry
The University of British Columbia
Vancouver, Canada

Date Nov 14/90

Abstract

The rate constants of the abstraction reaction $\text{Mu} + \text{HBr} \rightarrow \text{MuH} + \text{Br}$ were measured using the well established μSR technique at TRIUMF. Measurements were made at various temperatures between 170 and 480 K, and fit to the Arrhenius equation both with and without an additional $T^{1/2}$ dependence. The rate constants obtained were $k(T) = (5.101 \pm 0.106) \times 10^{-11} \exp\{-(0.560 \pm 0.110) \text{ kcal mol}^{-1}/RT\}$ and $k(T) = (0.183 \pm 0.005) \times 10^{-11} T^{1/2} \exp\{-(0.286 \pm 0.014) \text{ kcal mol}^{-1}/RT\} \text{ cm}^3 \text{ molecule}^{-1} \text{ s}^{-1}$. The low activation energy for such an exothermic reaction indicates that the barrier on the $\text{Mu} + \text{HBr}$ surface is early. Kinetic isotope effects of the $\text{H}/\text{Mu} + \text{HBr}$ reactions along with a lack of curvature in the $\text{Mu} + \text{HBr}$ Arrhenius plot suggest that tunneling is relatively unimportant down to 170 K.

Table of Contents

Abstract	ii
List of Tables	v
List of Figures	vi
Acknowledgement	vii
1 Introduction	1
2 μSR Technique	6
2.1 Muons and Muonium	6
2.2 Muon Spin Rotation	7
2.3 Muonium Spin Rotation	12
3 Bimolecular Reaction Kinetics	21
3.1 Introduction	21
3.2 Bimolecular Reaction Rates	21
3.3 Bimolecular Collision Theory	23
3.4 Potential Energy Surfaces	25
3.5 Transition State Theory	28

3.5.1	Variational Transition State Theory	35
3.5.2	Tunneling in Transition State Theory	35
3.6	Kinetic Isotope Effects	38
4	Experimental Setup	44
4.1	The Gas Target	45
4.2	Data Acquisition	46
4.3	Data Analysis	48
4.4	Sample Preparation and Analysis	49
5	Results and Discussion	52
5.1	Results	52
5.2	Previous Results	57
5.2.1	Mu + X ₂	57
5.2.2	H(D) + HBr	59
5.3	New Data: Mu + HBr	66
6	Conclusion	73
	Bibliography	75
	A Data	80

List of Tables

2.1	Properties of Muonium.	8
5.1	Experimental rate constants for $\text{Mu} + \text{HX}$	54
5.2	Saddle point characteristics of the H_2Br PES.	61
5.3	Kinetic parameters of the $\text{H}(\text{D}) + \text{HBr}$ system	64
5.4	Experimental and theoretical reaction rate constants of the $\text{H}(\text{D}) + \text{HBr}$ system	65
5.5	A comparison of data for the $\text{Mu}(\text{H},\text{D}) + \text{HBr}$ reactions . .	67

List of Figures

2.1	μ SR spectra of muonium in 1 atm N_2 and 6 Gauss.	19
2.2	Breit-Rabi diagram for the eigenenergies of muonium in an applied field in a vacuum.	20
3.1	Schematic Arrhenius plot.	39
4.1	Experimental setup of the target and surrounding apparatus.	51
5.1	Arrhenius plot of $Mu + HBr$, fit to $k = Ae^{-E_a/RT}$	55
5.2	Arrhenius plot of $Mu + HBr$, fit to $k = BT^{1/2}e^{-E_a/RT}$	56
5.3	Arrhenius plots for $Mu + X_2$	58
A.1	HBr in N_2 , 166 ± 3 K.	81
A.2	HBr in N_2 , 172 ± 5 K.	82
A.3	HBr in N_2 , 210 ± 2 K.	83
A.4	HBr in N_2 , 212 ± 4 K.	84
A.5	HBr in N_2 , 231 ± 10 K.	85
A.6	HBr in N_2 , 242 ± 2 K.	86
A.7	HBr in N_2 , 296 ± 1 K.	87
A.8	HBr in N_2 , 296 ± 1 K.	88

A.9 HBr in N ₂ , 306 ± 2 K.	89
A.10 HBr in N ₂ , 376 ± 1 K.	90
A.11 HBr in N ₂ , 380 ± 1 K.	91
A.12 HBr in N ₂ , 421 ± 2 K.	92
A.13 HBr in N ₂ , 475 ± 1 K.	93

Acknowledgement

I would like to thank my supervisor, Donald G. Fleming, without whom this thesis would not have been possible. I am equally indebted to our group who provided both moral and technical support and were absolutely vital to the experiment—Masa Senba, Alicia Gonzalez, James Pan, Donald Arseneau, and James Kempton, who were always available and ready to help when I needed them. I am indebted to Keith Hoyle and Curtis Ballard for their technical abilities and superior joke-telling skills. Without the co-operative efforts of all those mentioned this thesis may never have ended.

My thanks goes out to Bradley Gibson for his eternal emotional support and his super drawing on page 45. Lastly, I must thank my family, Herbert, Heather, and James Tempelmann, and friends, Kathy Martin and Alexander Kachura for something, but I'm not sure what.

Chapter 1

Introduction

In 1957 the first experiment to study the parity-violating asymmetric decay of the muon was completed [1]. This marked the beginning of the development of the μ SR technique which is used today for a variety of purposes [2], and specifically for the study of chemical reaction kinetics in this thesis [3,4]. Shortly after this important discovery, it was found that polarization of muons varied with different condensed media in which they stopped. Swanson [5], using positronium as a model, explained this behaviour by proposing the formation of muonium ($\text{Mu} = \mu^+e^-$), a positive muon bound to an electron captured from the surrounding medium. The muonium atom's significance in the field of chemical kinetics lies in its remarkably similar properties to the hydrogen atom, allowing it the status of an isotope of hydrogen. Thus, any reaction which can be accomplished using H is also possible with Mu, although reaction rate measurements may be limited by the lifetime (2.2 μs) of the muon as well as the time and frequency resolution of the μ SR technique, as in any other method of analysis.

But, as will be seen, the study of reactions with muonium provides unique information on the effects of isotopic mass changes on chemical kinetics, notably zero-point energy effects, and the quantum mechanical (QM) behaviour of reacting chemical species, which simply cannot be obtained to the same degree using H, D, or T. In particular, the Mu atom often provides unique information concerning the role of quantum tunneling in reaction kinetics.

Although we think of quantum mechanics as a relatively new field of study, as early as the 1920's kineticists were considering tunneling mechanisms (quantum mechanical processes) as additional contributions toward classical reaction rates [6]. As it turns out, quantum mechanical effects are most evident in reactions involving light atom transfer, such as the $\text{H} + \text{X}_2$ ($\text{X} = \text{I}, \text{Br}, \text{Cl}$) systems first studied experimentally by Bodenstein [7, 8] at the turn of the century, and most recently as $\text{Mu} + \text{X}_2$ by Gonzalez et al. [9]. Investigations were extended to the reactions of hydrogen with the hydrogen halides by Eyring and Polanyi's [10] calculation of the potential energy surface (PES) of H_2Br using their newly formulated and now well-known London-Eyring-Polanyi (LEP) method. The $\text{H} + \text{HX}$ ($\text{X} = \text{F}, \text{I}, \text{Cl}, \text{Br}$) systems are particularly interesting for several reasons. From an applications standpoint, HBr is a good flame inhibitor and it is hoped that reaction rate studies will help to explain this phenomenon [11, 12]. However, the true motivation for efforts to uncover the kinetic properties of these reactions is more strongly founded in a desire to

better understand the dynamics itself, especially where quantum mechanical processes are at work. The $\text{H} + \text{HBr}$ reaction is the most asymmetric system yet modelled by quantum scattering theory by virtue of both the presence of the heavy Br atom (as opposed to the extensively studied $\text{H} + \text{H}_2$ system), and by the uneven profile of the PES [13]. It thus provides a more stringent test of theoretical quantum methods used to predict experimental reaction rates. In addition to this, the exothermic nature of the $\text{H} + \text{HBr}$ abstraction reaction allows the investigation of vibrational population inversion which would not be possible with the highly endothermic $\text{H} + \text{HF}$ reaction under thermal conditions [13]. It is this phenomenon, also important in the study of $\text{H}(\text{Mu}) + \text{F}_2$, on which some chemical lasers are based.

Thermodynamic properties of the $\text{H} + \text{HX}$ series of reactions vary widely for each halogen (F, I, Cl, Br). Even though the kinematics of reaction is affected little by substitution of different halogens, the structure of the PES strongly influences thermodynamic properties such as the heat of reaction, which is endothermic for HF, about thermoneutral for HCl, exothermic for HBr, and highly exothermic for HI [14]. This makes possible the direct observation of the effect the PES topography has on the dynamic nature of reaction [14], specifically the effect of barrier height and position on quantum mechanical tunneling. Although an exact PES for the $\text{H} + \text{HBr}$ abstraction reaction has not been calculated, this system, as

well as its isotopic analogues, has been intensely investigated both experimentally [11, 12, 15–17] and theoretically [13, 14, 18–26] in an attempt to adequately predict quantum mechanical effects in other systems, such as tunneling which, as noted, is most easily recognized in light atom transfer reactions. The primary motivation of the work presented in this thesis was to provide experimental kinetic data which could, in principle, more profoundly express the quantum characteristics of the $\text{H} + \text{HBr}$ reaction than ever before. Replacement of the H atom with a muonium atom (i.e. $\text{Mu} + \text{HBr}$) is the ideal choice to this end due to muonium's mass being $1/9$ that of hydrogen. If tunneling is indeed important in this reaction, the ultra-light Mu atom should easily tunnel through the barrier at low temperatures, enhancing any QM effects already present in the $\text{H(D)} + \text{HBr}$ reaction, but perhaps only observable at very low temperatures where classical motion over the reaction barrier is suppressed.

The experiments completed for the purpose of this thesis measured the sum of abstraction and exchange rate constants for the reaction of $\text{Mu} + \text{HBr}$ over a range of temperatures extending down to 170 K. From this data the activation energy and preexponential factor, as defined by the Arrhenius equation, were calculated. Other than some preliminary measurements done in 1978 [3] and the results obtained in this thesis, no experimental or theoretical data presently exists for this system. Qualitative estimates of the kinetics of reaction were made possible using previous theoretical and experimental data obtained for the $\text{H(D)} + \text{HBr}$ reaction,

whose PES is applicable to all isotopic variants. It is hoped that the results presented here will encourage theorists to investigate the $\text{Mu} + \text{HBr}$ reaction and gain more insight into how to successfully model quantum effects in the field of chemical reaction kinetics.

Chapter 2

μ SR Technique

2.1 Muons and Muonium

Naturally occurring pions and their decay products, muons, are found in the ever-present cosmic radiation hitting the earth. Muons are elementary particles of the lepton family, which were first seen in cloud chamber experiments done in the late 1930's [27,28].

Muons may have positive or negative charge and are created through the natural decay of pions.

$$\pi^{+/-} \longrightarrow \mu^{+/-} + \nu_{\mu}/\bar{\nu}_{\mu} \quad (2.1)$$

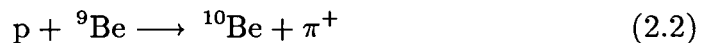
Since μ SR chemistry primarily uses the positive muon as its probe, this discussion will concentrate on the properties of the μ^+ . The positive muon, although lighter, behaves much like a proton. It's mass is 207 times greater than that of an electron and 1/9 the mass of a proton.

Muonium is formed through the capture of an electron by the positive muon, creating an atomic bound state (μ^+e^-). Because the muon

is very much heavier than the electron it is virtually a stationary nucleus with respect to the bound electron, thus satisfying the Born-Oppenheimer approximation [30]. As can be seen in Table 2.1, the reduced mass, Bohr radii, and ionization potentials of muonium and hydrogen are nearly identical. It is these similarities which allow us to treat muonium as an isotope of hydrogen. Since muonium is 1/9 the mass of hydrogen the observable isotope effect is more profound than that seen with either deuterium or tritium.

2.2 Muon Spin Rotation

Muons are created through the natural decay of pions. The production of pions outside the nucleus requires a nuclear collision with at least as much energy as the pion rest mass of $140 \text{ MeV}/c^2$. At TRIUMF, pions are typically created by bombarding a beryllium target with a 500 MeV proton beam.



The resulting pion decays with a mean lifetime of 26 ns emitting a muon and a neutrino as its daughter products.



Pion decay as shown is exoergic by 33.9 MeV, providing muons of 4.2 MeV energy in the pion rest frame. The corresponding muon momentum is $29.8 \text{ MeV}/c$.

Table 2.1: Properties of Muonium^a.

Mass	0.1131 m_H
	207.8 m_e
Reduced Mass	0.9952 m_e
	0.9956 μ_H
Bohr Radius	0.5315 \AA
	1.0044 (a_o) _H
Ionization Potential	13.54 eV
	0.9956 IP _H
Mean Thermal Velocity ^b	$7.5 \times 10^3 \text{ m s}^{-1}$
	2.967 \bar{v}_H
Hyperfine Frequency ^c	$2.8044 \times 10^{10} \text{ rad s}^{-1}$
	3.1423 ω_{oH}

a) Taken from Arseneau [29].

b) at 300 K.

c) in vacuum.

Pion decay is a parity violating process. The pion has a spin of zero, and all neutrinos are known to have negative helicity [31]. Simple angular momentum conservation then guarantees the production of positive muons with 100% polarization (negative helicity). The well defined spin of the muon is a crucial element of the μ SR technique, as will be seen later.

Muons produced through in-flight decay of pions have large, widely distributed energies and are unsuitable for studying μ SR chemistry in the gas phase, particularly at low (~ 1 atm) pressures. For such studies surface muons, those produced by pions decaying on the surface of the (Be) production target, are much more suitable. Surface muons are monoenergetic at 4.2 MeV. They are 100% longitudinally polarized and hence have a well defined stopping distribution with a range of ~ 150 mg cm $^{-2}$ in air [2]. This corresponds to a distance of ~ 30 cm in Ar gas at ~ 1 atm, after allowing for beamline windows and the muon counter (described below). These muons are transported to the target by a secondary beamline which focuses the beam, selects the appropriate momentum for the experiment, and if necessary rotates the spin direction of the incoming muons.

Since the positive muon has a non-zero angular momentum, it also has associated with it a magnetic moment, μ_l , whose direction is opposite to that of the angular momentum vector [2]. The magnetic moment is dependent on the angular momentum, \mathbf{L} , given by

$$\mu_l = -\frac{g_l \mu_B}{\hbar} \mathbf{L} \quad (2.4)$$

where $\mu_B (= e\hbar/2mc)$ is the Bohr magneton, and g_l is the orbital g factor.

In an external magnetic field, \mathbf{H} , a torque vector perpendicular to both the field and magnetic moment vectors exists such that

$$\mathbf{T} = \boldsymbol{\mu}_l \times \mathbf{H}. \quad (2.5)$$

By combining Equations (2.4) and (2.5) the expression for torque becomes

$$\mathbf{T} = -\frac{g_l \mu_B}{\hbar} \mathbf{L} \times \mathbf{H}. \quad (2.6)$$

If we apply Newton's law of motion to the above equation the result is

$$\frac{d\mathbf{L}}{dt} = \mathbf{T} = -\frac{g_l \mu_B}{\hbar} \mathbf{L} \times \mathbf{H}. \quad (2.7)$$

Since $d\mathbf{L}$ is perpendicular to \mathbf{L} , the magnitude of \mathbf{L} remains constant and the change in \mathbf{L} is manifest in direction only, resulting in the precession of the muon spin about the field axis. The Larmor frequency of precession is defined by the angle, ψ , swept out by vector \mathbf{L} in the plane of $d\mathbf{L}$ over time dt , thus given by

$$\omega_L = \frac{d\psi}{dt} = \frac{d\mathbf{L}}{L \sin \theta dt} = \frac{g_l \mu_B L H \sin \theta}{\hbar L \sin \theta} = \frac{g_l \mu_B}{\hbar} H. \quad (2.8)$$

The Larmor frequency of the muon is 13.55 KHz G^{-1} [30].

Like the pion which preceded it, the muon decays via the weak interaction, but with a lifetime of 2.2 μ s according to the decay scheme

$$\mu^+ \longrightarrow e^+ + \nu_e + \bar{\nu}_\mu. \quad (2.9)$$

This parity-violating process results in a positron being emitted preferentially along the direction of the muon spin axis. The decay positron is

detected at a fixed angle by an array of plastic scintillators (a positron ‘telescope’). The greatest number of positrons are counted when the muon spin precesses to a position pointing directly at the detector. Conversely, the minimum number of positron events are recorded when the muon spin is directed away from the detector. It is precisely this precession of the muon spin which causes the characteristic oscillation seen in a typical μ SR histogram (see Figure 2.1).

In practice, not all of the decay positrons are emitted exactly along the muon spin direction. The number of positrons emitted at a specific angle to the muon spin direction θ is given by in the expression

$$\frac{N(\theta)}{N} = 1 + A_\mu \cos \theta \quad (2.10)$$

where N is the total number of positrons emitted at all angles. Positrons from muon decay (at rest) are emitted over a range of energies from 0.0–52.8 MeV. If it were possible to detect all positrons with equal efficiency and the muon was 100% polarized at the time of its decay, the value of A_μ would be 1/3 [31]. In actual fact the muon beam may not be 100% polarized, or the muon may have suffered some depolarization during its slowing down process [32]. In addition, higher energy positrons are more efficiently detected than their low energy counterparts. Thus, A_μ may vary significantly during a single experiment and must be determined empirically for each run.

The observed muon decay signal is fit to a time dependent expression

for the number of positron events which have occurred,

$$N(t) = N_0 e^{-t/\tau} [1 + A_\mu \cos(\omega_\mu t + \phi_\mu)] + B \quad (2.11)$$

where τ is the average muon lifetime of 2.2 μ s, ω_μ is the Larmor precession frequency of the muon ($\omega_\mu = \gamma_\mu H$, where $\gamma_\mu = 13.55 \text{ KHz G}^{-1}$), ϕ_μ is the initial phase angle between the muon and the detector direction, N_0 is a normalization factor, B is the time independent background term, and t is the time each muon spends in the target before decaying. [Note that $(\omega_\mu t + \phi_\mu)$ is equal to θ in Equation (2.10).] It is critical that there be only one muon in the target at any one time; this is guaranteed by the electronic logic (see below). Without this requirement it would be impossible to obtain a well-defined time of decay for each individual muon.

2.3 Muonium Spin Rotation

In virtually all materials, excepting metals, muons are able to capture electrons as they pass through the material, forming what is known as a muonium atom ($\text{Mu} = \mu^+ e^-$) [2,4,32]. As stated earlier, muonium may be treated as a light H-atom, as evidenced by their remarkably similar properties listed in Table I. As with the muon itself, the study of chemistry, and particularly chemical reactions involving muonium is usually carried out within an external transverse magnetic field in order to facilitate muonium precession. Unlike the bare muon (or any muon in a diamagnetic environment), there are now two interactions which must be considered in describing the

precession of the muonium atom—the Zeeman and hyperfine interactions. The Zeeman interaction refers to the coupling of each individual particle in the atom (in this case one muon and one electron) to the external magnetic field. The hyperfine interaction describes coupling between the muon and electron themselves, and is independent of the external magnetic field applied. The spin Hamiltonian of the muonium atom can be written in the form

$$\mathcal{H}_{\text{Mu}} = \frac{\hbar\omega_o}{4}\hat{\sigma}_\mu \cdot \hat{\sigma}_e + \frac{\hbar}{2}\boldsymbol{\omega}_\mu \cdot \hat{\sigma}_\mu + \frac{\hbar}{2}\boldsymbol{\omega}_e \cdot \hat{\sigma}_e \quad (2.12)$$

where

$$\hbar\boldsymbol{\omega}_\mu = g_\mu\mu_o^\mu\mathbf{H}$$

$$\hbar\boldsymbol{\omega}_e = g_e\mu_o^e\mathbf{H}$$

$$\mu_o = \frac{e\hbar}{2mc} \text{ (magneton).}$$

The values of g_μ and g_e are -2 and 2 , respectively, with \mathbf{H} being the applied magnetic field. The first term in Equation (2.12) describes the hyperfine interaction, while the last two are the Zeeman interaction terms.

The muon and electron each have a spin of $\frac{1}{2}$. Thus, muonium can be formed in one of two possible spin states: an antiparallel ('singlet') state in which the electron and muon are paired ($|\alpha_\mu\beta_e\rangle$) and a parallel (triplet) state in which the electron and muon are unpaired ($|\alpha_\mu\alpha_e\rangle$). The four possible total spin ($S = 0, 1$) eigenstates of the muonium atom solutions of

Equation (2.12) are

$$S = 1 \begin{cases} |11\rangle = |\alpha_\mu\alpha_e\rangle \\ |10\rangle = s|\alpha_\mu\beta_e\rangle + c|\beta_\mu\alpha_e\rangle \\ |1-1\rangle = |\beta_\mu\beta_e\rangle \end{cases} \quad (2.13)$$

$$S = 0 \begin{cases} |00\rangle = c|\alpha_\mu\beta_e\rangle - s|\beta_\mu\alpha_e\rangle \end{cases} \quad (2.14)$$

where

$$\begin{aligned} c &= \frac{1}{\sqrt{2}}[1 + \delta]^{1/2} \\ s &= \frac{1}{\sqrt{2}}[1 - \delta]^{1/2} \\ \delta &= \frac{x}{\sqrt{1 + x^2}} \\ x &= \frac{(\omega_e + \omega_\mu)}{\omega_o} = \frac{H}{H_o} \end{aligned}$$

with $H_o = 1585$ G (compare to 500 G for the H atom). Because the incoming muons are polarized, and each has equal probability of capturing an unpolarized electron with either its spin up or spin down, it is assumed that the parallel and antiparallel states of muonium are formed in a 1:1 ratio.

In the case where no external field is applied, the Zeeman terms of the Hamiltonian are zero and the energies of the muonium triplet states

are degenerate such that

$$E_{S=1} = \frac{\hbar\omega_o}{4} \quad (2.15)$$

and

$$E_{S=0} = -\frac{3\hbar\omega_o}{4} \quad (2.16)$$

The transition energy between triplet and singlet states is $\hbar\omega_o$ ($= h\nu_o$, where $\nu_o = 4463$ MHz). This corresponds to a time of 0.224 ns and is usually not resolved in most applications of the μ SR technique, including that in this thesis, with a time resolution typically of ≥ 1 ns. In comparison, the corresponding transition in the H atom is 1420 MHz, well known in the field of radio astronomy [33].

The Breit-Rabi diagram shown in Figure 2.2 illustrates the field dependence of the energy splittings of the $S = 1$ and $S = 0$ states of muonium. In a transverse field the usual selection rules apply ($\Delta M = \pm 1$) resulting in four possible energy transitions indicated in Figure 2.2 (ν_{12} , ν_{23} , ν_{14} , ν_{34}). However, ν_{14} and ν_{34} are typically of order of ν_o and are thus not resolvable, leaving only the lower transitions, ν_{12} and ν_{23} of triplet muonium. Classically it can be reasoned that since singlet muonium has a spin of zero, there is no coupling of magnetic moment to the transverse magnetic field, and thus no precession of muonium in this state. Conversely, triplet muonium has a spin of one and will precess in a transverse magnetic field. It is further convenient that at fields < 10 G these transitions become degenerate making only one single coherent muonium precession frequency visible at a

frequency of $103\nu_\mu$ or 1.396 MHz G^{-1} . It is noted that, due to the electromagnetic moment, the precession of muonium is in the opposite direction to that of the bare muon.

The general equation describing the time dependent polarization of the μ^+ in the muonium atom in a transverse field is rather detailed and will not be derived, but just stated here as

$$P_\mu(t) = \frac{1}{4}[(1 - \delta)(e^{i\omega_{14}t} + e^{i\omega_{23}t}) + (1 + \delta)(e^{i\omega_{12}t} + e^{-i\omega_{34}t})] \quad (2.17)$$

where $\omega_{ij} = \omega_i - \omega_j = 2\pi\nu_{ij}$, and δ has been defined above [30]. The subscripts of the frequencies, ω_{ij} , are assigned in accordance with the assignments used on the Breit-Rabi diagram in Figure 2.2.

In weak fields on the order of 100 G it can be assumed that $x = 0$ (recall $x = H/H_0$, $H_0 = 1585 \text{ G}$), and hence $\delta \simeq 0$. By evaluating the real part of Equation (2.17) under very weak field conditions the following result for the time dependent muon polarization in muonium is obtained:

$$\text{Re } P_\mu(t) = \frac{1}{2} \cos \omega_M t \cos \Omega t + \frac{1}{2} \cos \omega_M t \cos(\omega_o + \Omega)t \quad (2.18)$$

where $\Omega = \frac{1}{2}(\omega_{23} - \omega_{12})$, and $\omega_M = \frac{1}{2}(\omega_{23} + \omega_{12}) = 1394H \text{ KHz}$. As stated earlier, $\omega_o (= 2\pi\nu_o)$ was unresolvable in the experiments described in this thesis. Coupling this point with the fact that $\Omega \simeq 0$ in magnetic fields on the order of $<10 \text{ G}$, Equation (2.18) may be further reduced to

$$\text{Re } P_\mu(t) = \frac{1}{2} \cos \omega_M t. \quad (2.19)$$

The result of these simplifications, which are thought of classically as the

coherent precession of triplet ($\alpha_\mu\alpha_e$) muonium, is an equation which accurately describes the experimental signal observed from μ^+ in the muonium atom in weak transverse fields

$$N = N_0 e^{-t/\tau} [1 + A_M e^{-\lambda t} \cos(\omega_M t + \phi_M) + A_\mu \cos(-\omega_\mu t + \phi_\mu)] + B. \quad (2.20)$$

This equation is of particular interest to the experiment discussed shortly. The second term in this expression accounts for any muons in diamagnetic environments bound to be present in the target vessel along with the desired muonium signal. The negative sign given to ω_μ merely reflects the opposed precession directions of muonium and μ^+ . In Equation (2.20), λ is a phenomenological relaxation rate of muonium, introduced to account for the interactions of the muonium atom with its environment. These may be caused by magnetic field inhomogeneities, spin exchange encounters, or chemical reaction of muonium with other species present. It is the latter which is of principle importance in this thesis.

The top of Figure 2.1 is a nice example of how a typical μ SR signal looks. It is customary to remove the normalization, background, and natural muon lifetime before fitting the modified signal to

$$S(t) = A_M e^{-\lambda t} \cos(\omega_M t + \phi_M) + A_\mu \cos(-\omega_\mu t + \phi_\mu). \quad (2.21)$$

This gives a plot much like that shown in the bottom of Figure 2.1, and is more illustrative when information about muonium relaxation is of paramount importance. Since this thesis is concerned with chemical relaxation

rates of muonium with HBr, the data will be shown in the latter form almost exclusively.

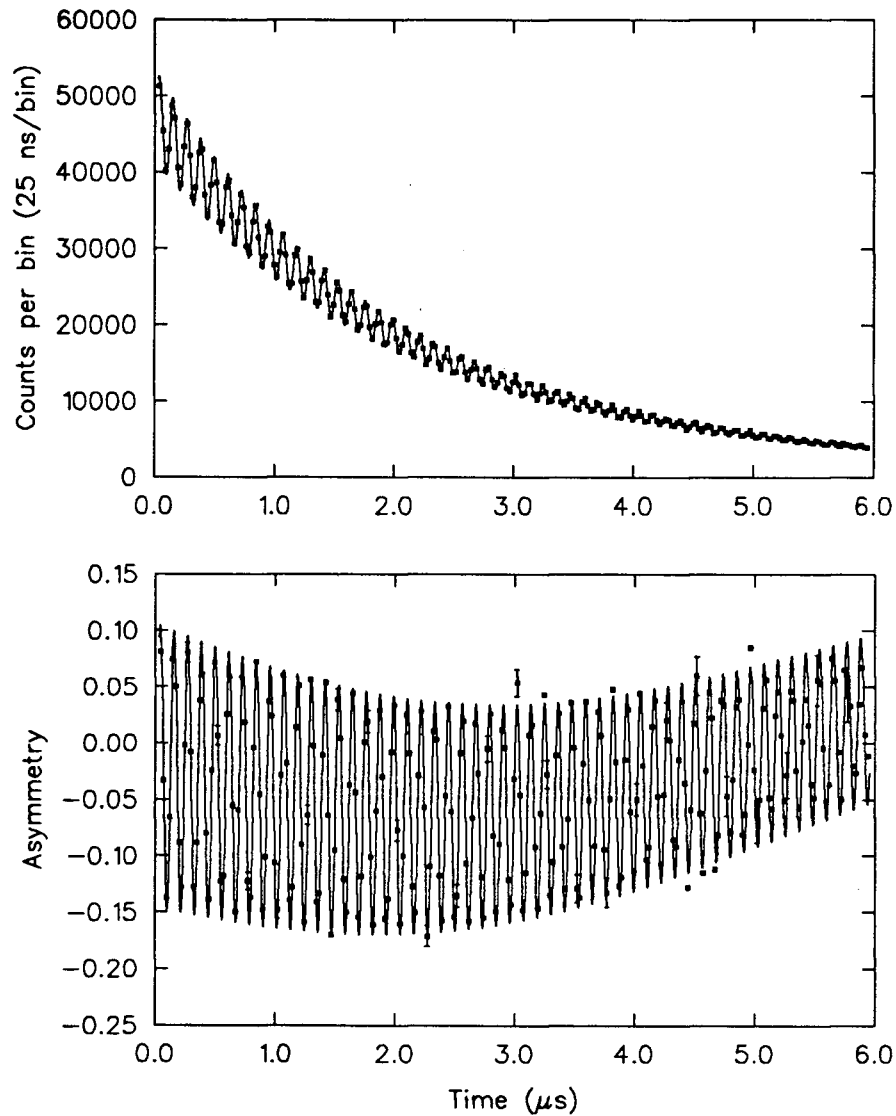


Figure 2.1: μ SR spectra of muonium in 1 atm N_2 and 6 Gauss. The top is a typical μ SR histogram fit to Equation (2.20). The exponential curve is due to the decay of μ^+ , which was removed to obtain the bottom histogram displaying the muonium signal (Equation (2.21)). The slow oscillation in the bottom histogram is due to μ^+ precession.

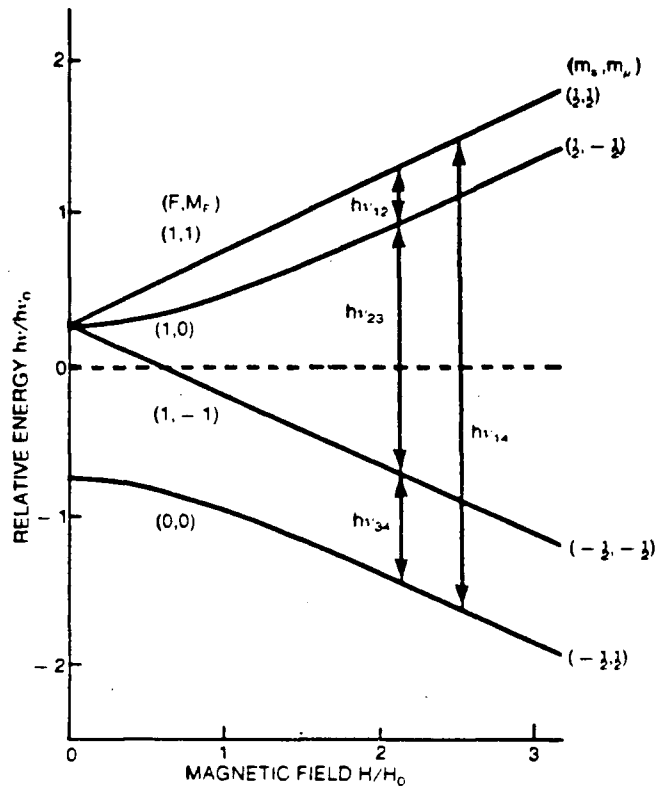


Figure 2.2: Breit-Rabi diagram for the eigenenergies of muonium in an applied field in a vacuum. At low fields, total-angular-momentum quantum numbers F and M_F describe the system. At high fields the muon and electron spins are decoupled and the individual quantum numbers, m_s and m_μ describe the system. The applied field is given in units of H_0 , which is 1585 Gauss. The frequency ν_0 is 4463 MHz.

Chapter 3

Bimolecular Reaction Kinetics

3.1 Introduction

The purpose of this thesis was to study the kinetic behaviour of the Mu + HBr system. In light of this, the following discussion focuses primarily on bimolecular reaction systems, of which Mu + HBr is just one example. Before discussing the results of this study, an overview of the kinetic theory used to interpret experimental kinetic data is essential. This includes a general discussion of bimolecular reaction rates, as well as brief introductions to potential energy surfaces (PES's), collision theory, and transition state theory (TST), and quantum mechanical effects.

3.2 Bimolecular Reaction Rates

An elementary bimolecular gas-phase reaction in a closed system can be represented by



where one molecule of A reacts with one molecule of B to form product molecules C and D. The molecularity of this reaction is 2, hence the name bimolecular. The bimolecular rate of reaction, \mathcal{R} , for the system described by Reaction (3.1) is given by

$$\mathcal{R} = -\frac{d[A]}{dt} = -\frac{d[B]}{dt}. \quad (3.2)$$

It is hardly surprising that some reactions have rates which are linearly proportional to concentrations of one or more reactant species present. This was discovered empirically, but by no means applies to all reactions. The general form of the equation for an elementary bimolecular reaction of the type (3.1) is

$$\mathcal{R} = k[A][B] \quad (3.3)$$

where k is the bimolecular reaction rate constant, and $[A]$ and $[B]$ are the concentrations of species A and B. Although for homogeneous kinetics k is independent of time and reactant concentration it has a temperature dependence which was first proposed by van't Hoff in 1884 [34] as

$$k = Ae^{-E_a/RT}. \quad (3.4)$$

Arrhenius used this equation to explain how reactions proceed with respect to temperature [35], hence its name—the Arrhenius equation. A is known as the preexponential factor, E_a is the activation energy of the reaction, T is absolute temperature, and R is the gas constant.

In fact, not all data can be fit to Equation (3.4) satisfactorily—several alternate equations have been proposed in an attempt to improve poor

agreement with experiment which consisted of various combinations of T^m and e^{cT} dependencies, where m and c are empirically determined constants (see Reference [36], p.43 for a brief list of rate constant equations). For a bimolecular reaction it is reasonable to let $m = 1/2$ in order to include the $T^{1/2}$ dependence observed in the bimolecular rate constant equation derived from simple collision theory (see Equation (3.12)).

$$k = BT^{1/2}e^{-E_a/RT} \quad (3.5)$$

A better fit for rate data of reactions whose E_a is very low is achieved using Equation (3.5), as in the case of $\text{Mu} + \text{HBr}$.

3.3 Bimolecular Collision Theory

The exact equation for the bimolecular rate constant of reaction is arrived at through the integration of the velocity dependent cross section over all molecular speeds. It is given by the expression

$$k(T) = \int_0^\infty f(T, v)\sigma(v)v dv \quad (3.6)$$

$$= 4\pi \left(\frac{\mu}{2\pi kT} \right)^{3/2} \int_0^\infty \sigma(v)v^3 e^{-\mu v^2/2kT} dv \quad (3.7)$$

or, by substituting $v = (2E_t/\mu)^{1/2}$, where E_t is the translational energy of the molecule, the expression becomes

$$k(T) = \left(\frac{8}{\pi\mu(kT)^3} \right)^{1/2} \int_0^\infty E_t\sigma(E_t)e^{-E_t/kT} dE_t \quad (3.8)$$

which is often more convenient when dealing with experiments whose cross section data is usually obtained in terms of collision energy. The function $f(T, v)$ is the Maxwell-Boltzmann distribution which describes the particle speed as a function of temperature, T ,

$$f(T, v)dv = 4\pi \left(\frac{\mu}{2\pi kT} \right)^{3/2} v^2 \exp\left(-\frac{\mu v^2}{2kT}\right) dv \quad (3.9)$$

where μ is the reduced mass of the system, v is its velocity, and k is the Boltzmann constant.

To solve this equation for $k(T)$, $\sigma(v)$ must be known exactly. Schatz [37] in fact has used exact QM calculations on an exact PES for the $\text{Mu} + \text{H}_2$ system, and hence determined the reactive cross sections and rate constants. Unfortunately, the $\text{H} + \text{H}_2$ system and its isotopic analogues are the only reactions for which an accurate PES has been calculated to date. Without such a surface, $\sigma(v)$ cannot be determined accurately.

The energy dependence of $\sigma(E_t)$ exists due to the possibility that colliding molecules do not always meet head-on, in which case the impacting molecule may not possess enough energy for reaction to occur. If all collisions were head-on it would be safe to assume that $\sigma(E_t)$ is constant so long as $E_t > E_0$, where E_0 is the threshold energy of the reaction. Since this is not true generally, the energy dependence of $\sigma(E_t)$ must be approximated. The 'line-of-centers' model assumes that for $E_t < E_0$

$$\sigma(E_t) = 0, \quad (3.10)$$

and for $E_t > E_0$

$$\sigma(E_t) = \frac{\pi d^2 (E_t - E_0)}{E_t} \quad (3.11)$$

where d is the sum of radii of the two colliding molecules. By substituting these values of $\sigma(E_t)$ into Equation(3.8) and evaluating the integral, the following expression for $k(T)$ is arrived at

$$k(T) = d^2 \left(\frac{8\pi kT}{\mu} \right)^{1/2} e^{-E_0/RT}. \quad (3.12)$$

Note that this equation has the same form as Equation (3.5). Recalling that the average relative molecular velocity is given by

$$\bar{v} = \left(\frac{8kT}{\pi\mu} \right)^{1/2}, \quad (3.13)$$

Equation (3.12) can be rewritten as

$$k(T) = \pi d^2 \bar{v} e^{-E_0/RT} \quad (3.14)$$

where $d = (r_A + r_B)$ for a simple 'hard sphere' model of colliding molecules, and $\sigma_0 = \pi d^2$ is the 'effective' cross section of reaction.

3.4 Potential Energy Surfaces

The bimolecular rate constant given by Equation (3.8) contains the principle feature of collision theory, namely $\sigma(E)$, and is essentially 'exact'. The cross section can be evaluated classically using trajectory theory or quantum mechanically. The most exacting test of the latter to date has been

the 3DQM calculations of Schatz [37] for the $\text{Mu} + \text{H}_2$ reaction on the accurate Liu-Siebahn PES for H_3 [38]. Schatz's calculations agree well with the TRIUMF experimental results [39]. One must have a PES to theoretically determine the cross section for reaction on the surface.

The potential energy surface was first introduced by Marcelin in 1914 [36,40], and in simple terms is a three dimensional picture of the potential energy of a reactive system as a function of the bond lengths of reactant and product species. This is most commonly presented in the literature as a relief map of contour lines marking regions of equal potential for the various bond distances. The reactive path of the system is thought to lie along the areas of minimum energy potential (MEP). However, trajectories across the surface may vary significantly depending upon the curvature of the PES and the QM nature of reaction. Determining the ideal reaction path (or paths if state-to-state cross sections are calculated) is important in obtaining true reaction rates. The reactant and product valleys meet one another at a col or saddle point, the region where the activated complex of the system resides.

PES's are determined empirically, semiempirically, as was first done by Eyring and Polanyi [10], or exactly for a limited number of simple systems, specifically the $\text{H} + \text{H}_2$ reaction and its isotopic variants, using *ab initio* calculations [38]. Solution of the Schrödinger equation, which is necessary for determining an exact PES, becomes difficult if not impossible for systems of many electrons, such as $\text{H} + \text{HBr}$. For such a reaction, semi-

empirical treatments are used which allow for parameter adjustment on the basis of experimental results rather than theoretical concepts.

Eyring and Polanyi used a method of calculation based on the London equation to determine PES's known as London-Eyring-Polanyi (LEP) surfaces. The London equation for a triatomic complex, ABC, expresses the potential energy, E , in terms of the coulombic energy integrals, $Q = Q_{ab} + Q_{bc} + Q_{ac}$, and exchange energy integrals α_{ab} , α_{bc} , and α_{ac} , of the complex.

$$E_{\pm} = Q \pm \frac{1}{2} \left[(\alpha_{ab} - \alpha_{bc})^2 + (\alpha_{bc} - \alpha_{ac})^2 + (\alpha_{ac} - \alpha_{ab})^2 \right]^{1/2} \quad (3.15)$$

This method seems to be useful only in making rough estimates of activation energies.

Sato [41] took the LEP method described above one step further in trying to eliminate the undesirable basin seen in the H_3 calculations. He used a modified version of the London equation

$$E_{\pm} = \frac{1}{1 + S^2} \left[Q \pm \frac{1}{2} \left[(\alpha_{ab} - \alpha_{bc})^2 + (\alpha_{bc} - \alpha_{ac})^2 + (\alpha_{ac} - \alpha_{ab})^2 \right]^{1/2} \right] \quad (3.16)$$

where he introduced an additional adjustable parameter S , the overlap integral. Known as a LEPS PES, this method is as empirical as the LEP method but conveniently gives potential surfaces free of basins. It's major disadvantage is that calculated barriers are too thin and may predict more QM tunneling than is true for reactions such as $H + H_2$.

The diatomics-in-molecules (DIM) treatment is another semiempirical method often used for PES calculation of H atom reaction with diatomic

molecules. The Hamiltonian is partitioned into separate operators for the diatomic and atomic fragments of the triatomic activated complex. The energies of the diatom and atom are then solved for variationally. DIM surfaces are used extensively in the treatment of the H + HBr system, and its isotopic variants since good descriptions of the diatomic fragments are readily available. For a more complete discussion of this method see Reference [42].

3.5 Transition State Theory

The concept of transition state theory (TST) was first envisioned and developed by Eyring [43], and Evans and Polanyi [44]. This was the first theory that treated a reaction in three continuous stages: reactant species, product species, and most important to the theory, the transition state species, otherwise known as the activated complex. Their initial ideas are now known as ‘conventional transition state theory’ (CTST), but the concepts generally apply to variational transition state theory (VTST), and quantum mechanical transition state theory (QM TST). Although CTST has been criticized in the past for its inability to predict reaction rates accurately, improvements, specifically the development of VTST, have allowed it to flourish. Fifty-five years after it was first envisioned, TST is still the method of choice for studying reaction kinetics, yielding particularly useful qualitative information.

Before going on to derive the TST rate equation of a bimolecular reaction it is necessary to discuss the assumptions and fundamental concepts involved. Initially, as stated earlier, the PES of the reaction system must be determined as accurately as is allowed by the complexity of the reactants and products. Herein lies one of the major challenges in the use of TST since, as pointed out by Truhlar et al. [45], at room temperature an error of 1 kcal mol^{-1} in the activation barrier of the PES causes an error of a factor ~ 5.6 in the rate constant. The error in k becomes even more pronounced at only slightly higher inaccuracies in the barrier height due to its exponential dependence in the error of the barrier. After obtaining the most accurate PES a reaction path leading from reactants and products, passing over the col or saddle point, is defined across the PES. Dividing surfaces, parallel to one another and separated by a very small distance δ , are drawn atop the col. It is in this transition state that the activated complex exists.

In describing the process which occurs as one moves from reactants to the activated complex and finally to the products (or in the opposite direction if one wishes), four assumptions were made which clearly define TST.

1) *Molecular systems which have surmounted the col may not turn back and reform reactant molecules.* This also applies to product molecules—once they have entered the transition state region they must exit out the reactant side of the PES. Clearly, the activated complex may not cross the

dividing surface more than once, however this is not always the case when one is dealing with a real reaction. Because TST counts all crossings of the dividing surface, even those where recrossing occurs sending the molecule back to its side of origin, calculated reaction rates tend to be too high when compared to experimental values [36].

2) *The energy distributions of reactant molecules follow the Maxwell-Boltzmann distribution. In addition, even when the system is not in the equilibrium state, the concentration of the activated state can be calculated using equilibrium theory.* This is often referred to as quasiequilibrium and is only valid provided assumption 1) is true, as explained by Laidler [36]. Suppose one is studying the forward reaction of molecules A and B, forming the activated complex X_f^\ddagger . Whether or not the system as a whole is in equilibrium is not important—the concentration of X_f^\ddagger will remain in equilibrium with the reactants even if products are removed because the activated complex has no choice but to continue moving towards the product state as required by assumption 1). The same argument applies to the backward reaction. It could be said that it is actually assumption 1) which allows one to calculate the concentration of the activated complex using equilibrium theory. It is not a classical equilibrium; addition of X_f^\ddagger to the system would disturb a classical equilibrium, but in the case of TST it does not.

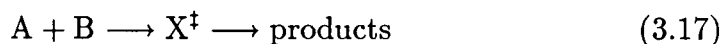
3) *It is permissible to separate the motion of the activated complex over the col from other motions of the molecule.* In actual fact, even in

classical theory this assumption is not entirely valid. There is some mixing of translational, rotational, and vibrational energies, and if there are anharmonic vibrations energy may flow between the molecule's normal modes of vibration. These errors are small. It is the consideration of quantized motion which introduces major problems of inseparability of the various motions of a molecule. In deriving the TST rate equation one assumes that the activated complex moves freely over the col. This is only possible if within the small distance δ (the transition state region) the potential energy curve is essentially flat. Johnston and Rapp [46] determined (from the PES) that δ of the $\text{H} + \text{H}_2$ system is no greater than ~ 30 pm. However, their calculated values of the de Broglie wavelengths ($\lambda = h/mv$, where m is the mass and v is the velocity of the species) for transfer of an H atom were 101 pm at 300 K, and 78 pm at 500 K. Since these values exceed the estimated value of δ it must be concluded that the motions of the $\text{H} + \text{H}_2$ system are inseparable.

4) *Chemical reaction can be treated in terms of classical motion over the reaction barrier, with quantum effects being ignored.* It has already been shown in assumption 3) that this not always valid. Besides difficulties with separability, quantized motion of the system introduces the concept of tunneling in which reactants which do not have enough energy to pass over the col merely penetrate the barrier to reach the product valley. The theoretical treatment of QM tunneling has proved to be one of the most challenging aspects of TST.

The rate equation for a bimolecular reaction has been derived in several ways using TST and principles of statistical mechanics. The methods most widely known are those of Wynne-Jones and Eyring [40], and Eyring [43], Evans and Polanyi [44]. These give exactly the same result, but are arrived at through different ideas concerning the motion of the activated complex over the col.

For a bimolecular reaction, such as



the equilibrium constant for the activated complex, K_c^\ddagger , is expressed in terms of the concentrations of A, B, and X^\ddagger in the form

$$\frac{[X^\ddagger]}{[A][B]} = K_c^\ddagger. \quad (3.18)$$

Note that Equation (3.18) is only true if assumption 2) is valid. Through statistical mechanics the equilibrium constant can also be expressed in terms of the partition functions of the reactant and transition state species such that

$$\frac{[X^\ddagger]}{[A][B]} = \frac{q^\ddagger}{q_A q_B} e^{-E_0^\ddagger/RT} \quad (3.19)$$

where q_A , q_B , and q^\ddagger are the partition functions of A, B, and X^\ddagger , respectively, and E_0^\ddagger is the difference in energy between activated complexes and reactants. From this point forward the arguments given by the theorists cited differ. Wynne-Jones and Eyring proposed that the motion of the activated complex over the col be treated as a very loose vibration. The

vibrational partition function is given (per degree of freedom) by

$$\frac{1}{1 - e^{-h\nu/kT}} \quad (3.20)$$

which describes the motion of the activated complex over the col. In order for the molecule to pass completely over the col the vibration responsible for its motion must have a frequency which approaches zero. This is achieved by taking the limit of Equation (3.20) as ν goes to zero:

$$\lim_{\nu \rightarrow 0} \frac{1}{1 - e^{-h\nu/kT}} = \frac{1}{1 - (1 - h\nu/kT)} = \frac{kT}{h\nu}. \quad (3.21)$$

By removing this portion from the the total partition function, q^\ddagger , a new partition function, q_\ddagger containing the remaining parts is defined by

$$q^\ddagger = \frac{kT}{h\nu} q_\ddagger. \quad (3.22)$$

Combining Equations (3.19) and (3.22), and rearranging gives

$$\nu[X^\ddagger] = [A][B] \frac{kT}{h} \frac{q_\ddagger}{q_A q_B} e^{-E_o/RT}. \quad (3.23)$$

The frequency, ν , on the left-hand side of the above equation represents the frequency at which X^\ddagger is converted into products. Clearly, $\nu[X^\ddagger]$ is the rate of conversion into products, namely \mathcal{R} . Furthermore, recalling Equation (3.3) ($\mathcal{R} = k[A][B]$) it is quickly recognized that the bimolecular rate constant, k , is given by

$$k = \frac{kT}{h} \frac{q_\ddagger}{q_A q_B} e^{-E_o/RT}. \quad (3.24)$$

Equation (3.24) is the CTST bimolecular reaction rate formula.

The same result is arrived at by arguing, as Eyring, and Evans and Polanyi did, that the motion over the col can be modelled by translational motion given by the expression of the translational partition function of a particle of mass m_{\ddagger} moving in a one dimensional box of length δ .

$$q_{\ddagger} = \frac{(2\pi m_{\ddagger} kT)^{1/2}}{h} \delta q_{\ddagger} \quad (3.25)$$

As with the preceding derivation, q_{\ddagger} represents the partition function of X^{\ddagger} with the partition function responsible for motion over the col removed. Combining Equations (3.19) and (3.25) gives

$$[X^{\ddagger}] = [A][B] \frac{(2\pi m_{\ddagger} kT)^{1/2}}{h} \delta \frac{q_{\ddagger}}{q_A q_B} e^{-E_o/RT}. \quad (3.26)$$

The frequency with which the molecules pass over the col is now given by their average relative velocity divided by the distance travelled, δ :

$$\nu = \frac{\bar{v}}{\delta} = \left(\frac{kT}{2\pi m_{\ddagger}} \right)^{1/2} \frac{1}{\delta}. \quad (3.27)$$

It is simple to show that, again, by evaluating $\nu[X^{\ddagger}] (= \mathcal{R})$ and equating this with Equation (3.3) one arrives at the identical result as given by the Wynne-Jones and Eyring derivation, namely Equation (3.24).

All the concepts so far discussed apply equally well to CTST and VTST. It should be noted that CTST models the reaction in a purely classical fashion. The energy difference between reactants and complexes does not account for their zero-point energies derived from quantum mechanics. Furthermore, the partition functions are taken to be separable, and with the exception of vibrational motion, are classically derived.

3.5.1 Variational Transition State Theory

Variational transition state theory (VTST), developed by Truhlar and co-workers, attempts to obtain more accurate reaction rate constants by considering various positions for the dividing surface along the MEP in its calculations. Since VTST is often a preferable treatment to CTST in its wider applicability and because it gives an upper bound to rate constants by minimizing recrossing effects, much has been written on the subject—those with further interest may consult References [36,45,47–49] for reviews by various authors.

The main premise supporting the development of VTST is that the transition state of the surface is defined at a position on the PES such that it gives a minimum rate constant. Since recrossing of the dividing surface gives inflated values of $k(T)$, a minimum value, as found using this method, will be closer to the true value than that calculated using CTST. It must also be noted that unlike CTST, the threshold energy in VTST includes zero-point energy shifts in the transition state and reactant species, which in fact are especially important in the study of kinetic isotope effects.

3.5.2 Tunneling in Transition State Theory

The quantum mechanical effects which influence the reaction rate constant of a system include QM tunneling and zero-point energy effects. These mass sensitive effects, called ‘kinetic isotope effects’ (KIE’s), are observed through isotopic substitution. It is a challenge to accommodate quantum

effects using TST as exact potential surfaces are so difficult to obtain. Despite this, theoretical studies have come closer to interpreting quantum mechanical reaction behaviour more accurately.

QM tunneling is loosely defined as the process by which particles with energy less than that of the potential barrier are still able to reach the product valley of the PES. Because, in most cases, the majority of particles have sufficient energy to pass over the col at room temperature and above, QM tunneling is best observed at low temperatures where classical motion over the barrier is no longer a competitor—the majority of molecules no longer have enough energy to surmount the col. Tunneling favours systems where light particles are being transferred (such as Mu) and where the reaction barrier is thin. So far, the QM aspects of reacting systems are still difficult to treat accurately using transition state theory, however, progress has been made in the past several years which shows promise. In many cases the mathematics applied in QM treatments is rather complicated. For further explanation see References [6, 47, 50–52].

TST is based on classical concepts, particularly the separation of motions of the reaction coordinate which violates the uncertainty principle. It is possible, in theory, to apply quantum theory to both the preexponential factor and the activation energy of the bimolecular rate constant. It was shown previously through TST that the preexponential factor is dependent on the partition functions of both reactants and activated complexes. If one were to quantize the translational and rotational partition functions (only

that of the vibrational energy is quantized) for the motions perpendicular to motion over the col it is conceivable that a more accurate value of A , and thus a more accurate rate constant could be calculated. At the very least one hopes to predict the extent of tunneling in a given reaction relative to reactions where tunneling is negligible. However, incorporating QM theory into TST is difficult and is usually done so on an ad-hoc basis.

QM effects are also manifest in the zero-point energy shifts of the reactant and transition state species. Quasiclassical trajectory theory (QCT) includes these zero-point energy shifts in the activation energy, E_a , of the rate constant equation (Equation (3.4)), but otherwise treats the motion over the col classically. This treatment has been used to calculate rate constants of the H + HX abstraction reaction [14,21].

Tunneling is evidenced to be important in reactions whose Arrhenius plot, a plot of $\ln k$ versus $1/T$, shows curvature, and finally levels off at low temperature (see Figure 3.1). This is expected since, theoretically, a particle with zero energy is still able to tunnel through the reaction barrier so long as the reaction valley is higher than that of the products especially for light atom transfer reactions. The Tolman definition clearly shows the dependence of E_a on temperature:

$$E_a(T) = \langle E^* \rangle - \langle E \rangle. \quad (3.28)$$

where $\langle E^* \rangle$ is the average energy of molecules undergoing reaction and $\langle E \rangle$ is the average energy of all reactant molecules [36]. The average translational energy of reactant molecules is $\frac{3}{2}kT$, whereas that of a colliding

molecule is $\sim 2kT$. Thus, $\langle E^* \rangle$ is greater than $\langle E \rangle$ by about $\frac{1}{2}kT$. When quantum tunneling dominates, $\langle E^* \rangle$ is reduced, notably at low temperatures for light atoms such as Mu, such that E_a is also reduced. It is this phenomenon which is responsible for the Arrhenius plot curvature at low T , particularly evident in some Mu atom reactions.

The Wigner threshold law defines the energy dependent cross section of reaction, $\sigma(E)$, by

$$\sigma(E) \propto (E - a)^{n/2} \quad (3.29)$$

where $n = -1$ and $a = 0$ for an exothermic reaction [53]. Substituting this approximation into the rate equation given by Equation (3.8), the proportionality

$$\lim_{T \rightarrow 0} k(T) \propto T^0 \quad (3.30)$$

is obtained showing that the rate constant of reaction is independent of temperature in the regime of Wigner threshold tunneling. Again, this is observable in the Arrhenius plot (see Figure 3.1) where sudden curvature marks the initial temperature below which tunneling becomes dominant. This threshold temperature can be roughly calculated if the barrier thickness is known, as will be done in Chapter 5.

3.6 Kinetic Isotope Effects

Kinetic isotope effects (KIE's) refer to the mass dependent changes in rates of reaction which occur when a reactant atom or molecule is replaced by its

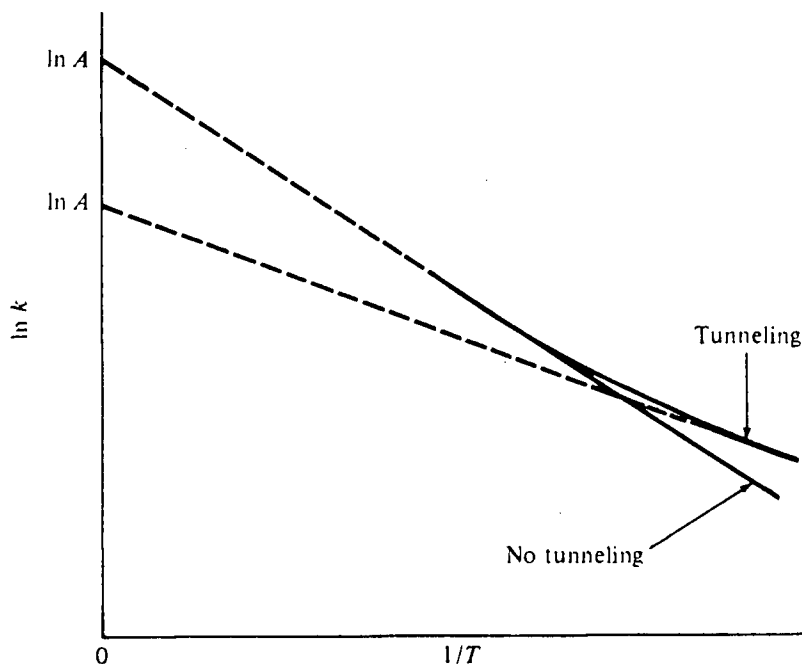


Figure 3.1: Schematic Arrhenius plot showing the curvature that arises if quantum mechanical tunneling is significant. Taken from Laidler [36].

isotope. KIE's are often divided into two types: primary effects and secondary effects. Primary effects are observed when the isotopic substituent is directly involved in bond breaking or formation during the reaction. Secondary effects are those observed in which the reacting bonds do not directly involve the replacement isotope. In the case of reaction between Mu and HBr we are concerned with primary isotope effects only as every atom present is directly involved in bonding processes.

There are three ways in which KIE's are seen in the rate constant

expression: through zero-point energies of the reactants and activated complexes, through the fact that lighter particles have a higher intrinsic probability of penetrating the reaction barrier, and finally, through the inverse square root proportionality between the mass of the species and its velocity (see Equation (3.13)). As one might expect, the largest isotope effects are witnessed when the difference in mass between the two isotopes is greatest. Clearly Mu, which is 1/9 the mass of H, will cause the greatest isotope effect when substituted for H, D, or T in reaction. The fact that Mu is substantially lighter (rather than heavier) than the others is also important since light atoms undergo quantum tunneling more readily than heavier atoms.

KIE's are often difficult to calculate accurately, especially when the reaction of interest involves large complex molecules. Reasons for this are that vibrational frequencies of activated complexes, which are the major contributors to KIE's owing to their dependence on the reduced mass of the molecule, are not easily determined and must often be approximated even for simple systems. In addition to this, reactions involving light atoms such as Mu are subject to QM tunneling which can markedly affect the observed rate constant, and subsequently the isotopic rate constant ratio. In fact, by comparing the experimental and theoretically calculated isotopic rate constant ratios the presence of QM tunneling can sometimes be confirmed.

Given two nearly identical molecules which differ only by one isotopic substituent, it can be approximated that there will be no difference in

the electronic energy levels of the two molecules. Additionally, because rotational and translational motions are accurately described using classical mechanics, they offer no contribution to kinetic isotope effects. The primary cause of KIE's in TST is the mass dependence of vibrational frequencies, ν_i , of the molecule which directly determine its zero-point energy level.

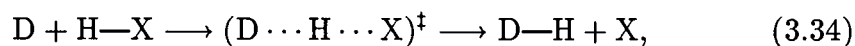
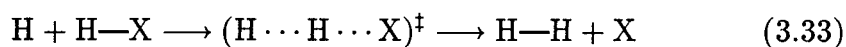
$$E_{\text{zero-point}} = \frac{1}{2}h\nu_i \quad (3.31)$$

The mass dependence arises in the classical harmonic oscillator expression for the vibrational frequencies of a molecule.

$$\nu_i = \frac{1}{2\pi} \sqrt{\frac{\kappa}{\mu_i}} \quad (3.32)$$

κ is the vibrational force constant which remains fixed despite substitution of one atom in the molecule with its isotope, and μ_i is the reduced mass of the molecule.

Given the following abstraction reactions involving H(D) and the hydrogen halides, or any heavier molecule for that matter,



the rate constants of Reactions (3.33) and (3.34) are given using TST (Equation (3.24)) by

$$k_{\text{H}} = \frac{kT}{h} \frac{q_{\ddagger}^{\text{H}}}{q_{\text{HX}}q_{\text{H}}} e^{-E_{\ddagger}^{\text{H}}/RT} \quad (3.35)$$

$$k_{\text{D}} = \frac{kT}{h} \frac{q_{\ddagger}^{\text{D}}}{q_{\text{HX}}q_{\text{D}}} e^{-E_{\ddagger}^{\text{D}}/RT}. \quad (3.36)$$

Combining Equations (3.35) and (3.36) the kinetic isotopic ratio (KIE) for the H/D abstraction reactions is

$$\frac{k_{\text{H}}}{k_{\text{D}}} = \frac{q_{\ddagger}^{\text{H}}}{q_{\ddagger}^{\text{D}}} \frac{q_{\text{D}}}{q_{\text{H}}} e^{-(E_{\text{c}}^{\text{H}} - E_{\text{c}}^{\text{D}})/RT}. \quad (3.37)$$

If the barrier to reaction is early such that the transition state species resembles reactants, there is no change in the partition functions of motion associated with isotopic substitution. Furthermore, factoring out the trivial $(1/m^*)^{1/2}$ dependence due to the velocity of the particle (see Equation (3.14)) the following expression is obtained

$$\frac{k_{\text{H}}}{k_{\text{D}}} = \frac{\kappa_{\text{H}}}{\kappa_{\text{D}}} \left[\frac{m_{\text{D}}^*}{m_{\text{H}}^*} \right]^{1/2} \quad (3.38)$$

where $\kappa_{\text{H}}/\kappa_{\text{D}}$ is known as the transmission coefficient ratio of reactions (3.33) and (3.34). Within the transmission coefficient ratio lies the exponential difference in activation energies of the isotopic reactions, which are strongly influenced by zero-point energy shifts. But again, for an early barrier whose transition state resembles reactants the zero-point energies of the transition state species remain essentially constant with isotopic substitution. Thus, the transmission coefficient ratio, under the condition of an early barrier, is a measure of the importance of QM tunneling in the reaction—a $\kappa_{\text{H}}/\kappa_{\text{D}} > 1$ indicates that tunneling may be important to reaction.

The treatment discussed here has been simplified such that only approximate predictions can be made. For a more accurate analysis of KIE's, especially those with barriers located centrally on the PES, a knowledge of

the PES of the specific reaction is necessary so that characteristics of the activated complex are available.

Chapter 4

Experimental Setup

The temperature dependent bimolecular rate constant of the reaction between HBr and muonium was determined through the measurement of muonium spin relaxation rates at various temperatures and pressures using the μ SR technique. Temperatures ranged from 170 K to 480 K. At each temperature the relaxation rate of $\text{Mu} + \text{HBr}$ was measured at several HBr concentrations up to 4×10^{17} molecule cm^{-3} . The moderator gas used was nitrogen. These measurements were made at TRIUMF, the meson facility at UBC. The proton beam at TRIUMF has an energy of 500 MeV and current of $\sim 100 \mu\text{A}$, and directed at a suitable target, in this case carbon or beryllium, results in the production of pions. ‘Surface’ muons, muons created by pion decay on the surface of the target, were used for this experiment on beamlines M15 and M20. Those interested in a more detailed account of the operation of TRIUMF can consult the TRIUMF Handbook.

The main requirements of this experiment, excluding the μ SR apparatus itself, were a target vessel and heating/cooling system which could

provide stable temperatures within the range discussed, a gas handling system capable of charging the target vessel with various controllable concentrations of HBr diluted by moderator gas, and a convenient means by which the concentration of HBr in the vessel can be accurately determined.

4.1 The Gas Target

It is well known that quantum tunneling is best observed at low temperatures [6]. For this reason it was required that we be able to measure relaxation rates from 480 K down to 170 K. These temperature constraints, as well as some of the μ SR technique itself, necessitated a carefully designed reaction vessel. In fact, it was discovered through off-line testing that separate high temperature and low temperature vessels were needed to complete the experiment. The low temperature target vessel consisted of three nested aluminum vessels. The innermost vessel held the target gas and had a volume of 13.7 l. This was surrounded by a temperature controlling jacket. The temperature of the vessel was monitored by an iron-constantan thermocouple located in a $\frac{3}{8}$ in. stainless steel tube, offset by several inches from the center of the target area. Heating of the inner vessel was accomplished by passing hot air through a simple heat exchanger and subsequently through the hollow jacket. Similarly, the reaction vessel was cooled using dry air, first passed through coils submerged in a large dewar of liquid nitrogen. By regulating the rate of flow of cold

air through the jacket it was possible to obtain stable temperatures as low as 100 K, with an error of less than 4%. A third vacuum jacket encased the heating/cooling jacket with the purpose of insulating the vessel and preventing ice from forming on the outer beam window at low temperatures. The muon beam passed through two kapton windows before stopping in the target material. Both windows were 0.0127 cm thick Kapton of 5 cm and 10.5 cm diameter for the inner and outer windows, respectively. The high temperature data, between 300 K and 500 K was obtained during an earlier experimental period. For this a 16.6 l nickel-plated copper target vessel was used to prevent HBr from reacting with the vessel walls. The vessel was wrapped with heating tape and insulation in order to obtain reaction temperatures up to 500 K. The muons entered the target through a single Kapton window of 0.0127 cm thickness (see Figure 4.1 for apparatus orientation).

4.2 Data Acquisition

Since the first μ SR experiment at TRIUMF was run in the early 1970's, the data acquisition system has gone through a variety of modifications, but the basic principle has remained the same. It is discussed in greater detail elsewhere [3]. For the purpose of this thesis only a brief explanation is required.

Before the muon enters the target window it must pass through a

collimator followed by a thin scintillation counter. The resulting pulse is processed and starts a high precision clock (TDC). On initially entering the target vessel the muon captures an electron from the moderator gas and subsequently thermalizes in a time estimated to be about 20 ns [54]. The resulting muonium atom precesses in a transverse field and undergoes radioactive decay after surviving for a mean lifetime of 2.2 μ s. The decay products are a positron and two neutrinos. The positron is detected by telescopic counters located above and below the target vessel (see Figure 4.1). In order for a ‘good’ event to occur the positron must be detected within about 7 μ s after the parent muon is ‘seen’ by the thin muon counter. If so, the clock is stopped, the bin corresponding to the time of decay is incremented, and the clock is reset. A PDP 11/34 computer was used to acquire and store the resulting histogram of number of events as a function of decay time. Events involving multiple detection of muons or positrons are rejected, as are muon counts without corresponding positron detection. In this case the acquisition system waits for a period of several muon lifetimes before resetting the clock and recording the next event.

The external transverse field applied in this experiment ranged from 4.5—7.5 Gauss. This is considered a very weak field in μ SR experiments.

4.3 Data Analysis

As stated previously, data was obtained in the form of number of events versus survival time of the muon. Such histograms were fit, using a multi-parametered χ^2 -minimization fitting routine [55], to Equation (2.20)

$$N(t) = N_0 e^{-t/\tau} [1 + A_M e^{-\lambda t} \cos(\omega_M t + \phi_M) + A_\mu \cos(-\omega_\mu t + \phi_\mu)] + B.$$

For display purposes the natural muon lifetime factor, $e^{-t/\tau}$, normalization N_0 , and the background, B , were subtracted out leaving the signal expressed in Equation (2.21),

$$S(t) = A_M e^{-\lambda t} \cos(\omega_M t + \phi_M) + A_\mu \cos(-\omega_\mu t + \phi_\mu).$$

The parameter of interest here is λ , the relaxation rate, which allows determination of the bimolecular rate constant of reaction, k . Several of the histograms obtained while using the nickel-plated reaction vessel retained a residual signal within the first fraction of a μs in the spectrum. This signal was due to the fast precession of muons in the walls of the nickel which provide a spurious magnetic field of ~ 1000 G. To obtain a more accurate fit, the nickel signal was isolated using four additional parameters. The relaxation of this contamination is closer to Gaussian than Lorentzian, making the actual equation used for fitting problem data the following:

$$N(t) = N_0 e^{-t/\tau} [1 + A_M e^{-\lambda t} \cos(\omega_M t + \phi_M) + A_\mu \cos(-\omega_\mu t + \phi_\mu) + A_N e^{\lambda_N^2 t^2 / 2} \cos(-\omega_N t + \phi_N)] + B$$

where A_N , λ_N , ω_N , and ϕ_N are the asymmetry, relaxation, precession frequency, and phase, respectively, of the muon signal from within the nickel-plated walls of the reaction vessel.

4.4 Sample Preparation and Analysis

HBr gas was obtained from Matheson and had a purity of 99.8%. Nitrogen, the moderator gas used, was obtained from Canadian Liquid Air and had a purity of 99.999%. It was necessary to ensure that oxygen was absent from the HBr gas since oxygen undergoes rapid electron spin exchange with muonium which would alter the relaxation rate observed. This was done by repeatedly freezing the HBr down to 78 K, pumping on the solid, and thawing. To load an HBr sample a small standard volume ($SV = 0.104$ l) was filled to the desired pressure with gas. At room temperature and below the gas was then forced into the target vessel with nitrogen until a total pressure of about 800 Torr was reached. However, at higher temperatures the total gas pressure was increased in order that the density of gas remained constant and equal to that at 298 K and 800 Torr. To more accurately determine the concentration of HBr present in the vessel two samples of known pressure were withdrawn after each run, dissolved in water and titrated with sodium hydroxide in the presence of phenolphthalein indicator. Off-line experiments confirmed that passivating the vessel with comparable concentrations of HBr for 10 minutes before each run resulted in

reasonable agreement between initial pressure measurements and titration values. Very good agreement was seen towards the end of the experiment when it can be presumed that the reaction vessel was well passivated.

Because the rate of reaction of $\text{Mu} + \text{Br}_2$ is substantially greater than that of $\text{Mu} + \text{HBr}$ (about 30 times greater at room temperature [9]) it was necessary to test the HBr gas for the presence of Br_2 . This was done using iodometry, a technique in which iodide ions reduce the Br_2 , and the resulting iodine is titrated with thiosulfate in the presence of starch indicator. The lower detection limit of Br_2 is 2×10^{-7} M, which is well below the concentration required to affect our measured rate constant. It was found that untreated HBr gas did contain trace amounts of Br_2 . To eliminate Br_2 from the sample, the lecture bottle was cooled to about 208 K before letting HBr into the standard volume. At this temperature Br_2 is a solid and has a vapour pressure of less than 0.0013 atm. This simple method proved effective for obtaining HBr free of Br_2 .

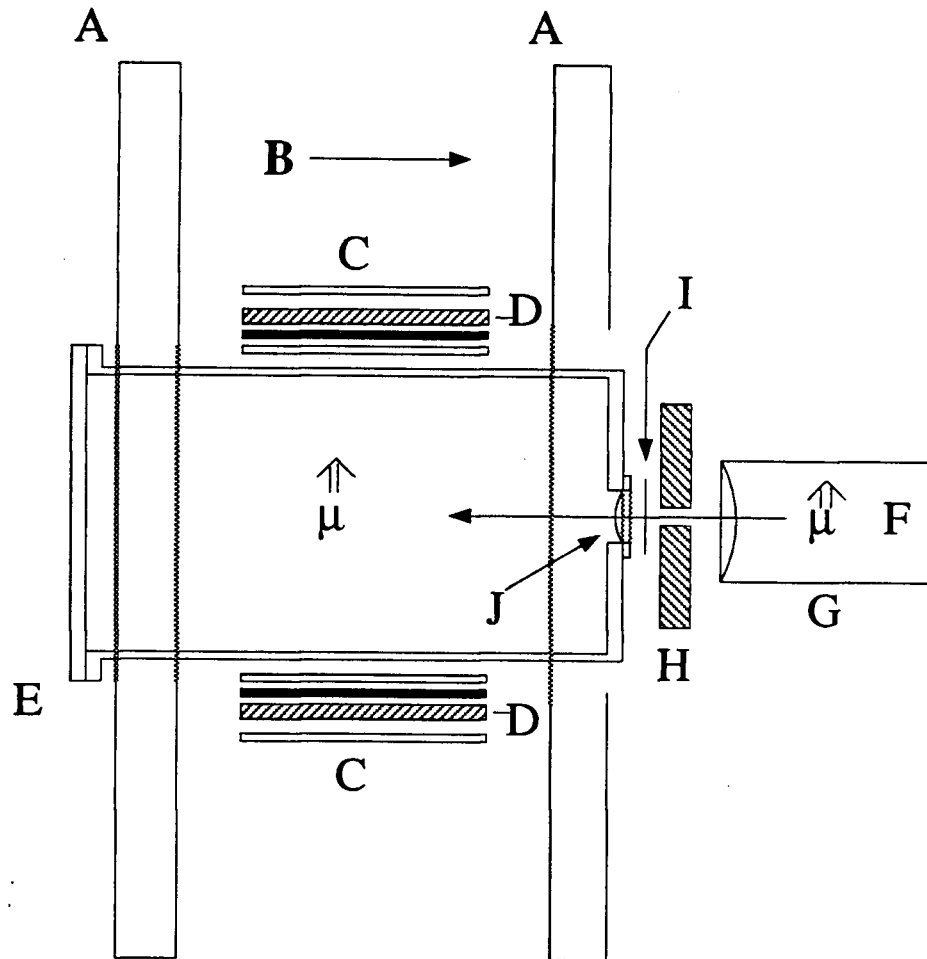


Figure 4.1: Experimental setup of the target and surrounding apparatus. The target vessel shown is a simplified version of the two vessels used, which are described in further detail in Section 4.1. A) helmholtz coils, B) magnetic field direction, C) counting telescopes, D) graphite, E) target vessel, F) μ^+ beam, G) beamline, H) brass collimator, I) thin muon counter, J) target vessel window.

Chapter 5

Results and Discussion

5.1 Results

The bimolecular rate constants for the reaction $\text{Mu} + \text{HBr}$ were obtained at temperatures in the range of 170–480 K. The $\text{Mu} + \text{HBr}$ reaction obeys the bimolecular rate equation (Equation (3.3)) such that the relaxation rate is linearly dependent upon the concentration of both Mu and HBr . However, the μSR technique demands that there be only one Mu atom in the reaction vessel at a time (see section 2.1) so that the relaxation rate is always pseudo first order related to the bimolecular rate constant by

$$\lambda([\text{HBr}]) = \lambda(0) + k[\text{HBr}] \quad (5.1)$$

where $\lambda(0)$ is the relaxation rate measured in the absence of HBr . k was obtained experimentally from Equation (5.1) by extracting $\lambda([\text{HBr}])$ from the μSR signal fit [55] to Equation (4.3) at concentrations ranging from about $4.0\text{--}40.0 \times 10^{16}$ molecule cm^{-3} . The plots of λ versus $[\text{HBr}]$ for all

temperatures measured, shown in Appendix A, confirm the linear relationship between reaction rate and reactant concentration of the Mu + HBr system, as demanded by Equation (5.1). These fits were modified linear regressions [56] which took account of error bars in the HBr concentration.

The measurements were done twice at all temperatures, except the two highest, to minimize error due to temperature fluctuation. The rate constants measured at each temperature are reported in Table 5.1. Maintaining a steady temperature was more difficult for those below room temperature, as reflected in the temperature errors listed in this table.

The temperature dependent rate constants were fit [57] to the Arrhenius equation in both the absence (Equation (3.4)) and presence (Equation (3.5)) of the $T^{1/2}$ dependency inherent in the average velocity reactants, and are illustrated in Figures 5.1 and 5.2 by plots of $\ln k$, and $\ln(k/T^{1/2})$ versus $1/T$. The values of E_a and A were found to be 0.560 ± 0.011 kcal mol⁻¹ and $5.101 \pm 0.106 \times 10^{-11}$ cm³ molecule⁻¹ s⁻¹ using Equation (3.4), and 0.286 ± 0.014 kcal mol⁻¹ and $0.183 \pm 0.005 \times 10^{-11}$ cm³ molecule⁻¹ s⁻¹ using Equation (3.5). The errors associated with these values indicate that a better fit was obtained using the latter equation, i.e. that including the $T^{1/2}$ dependence. This is not surprising in light of the fact the E_a found from the usual Arrhenius expression is so small (on order of kT).

Table 5.1: Experimental rate constants for Mu + HX

T (K)	k (10^{-11} cm ³ molecule ⁻¹ s ⁻¹)	Reaction vessel
475 ± 1	3.054 ± 0.107	Ni
421 ± 2	2.708 ± 0.061	Ni
380 ± 1	2.699 ± 0.091	Ni
376 ± 1	2.110 ± 0.054	Ni
306 ± 2	2.115 ± 0.040	Al
296 ± 1	1.926 ± 0.061	Ni
296 ± 1	1.702 ± 0.054	Ni
242 ± 2	1.615 ± 0.040	Al
231 ± 10	1.563 ± 0.032	Al
212 ± 4	1.381 ± 0.028	Al
210 ± 2	1.247 ± 0.028	Al
172 ± 5	1.055 ± 0.021	Al
166 ± 3	1.015 ± 0.021	Al

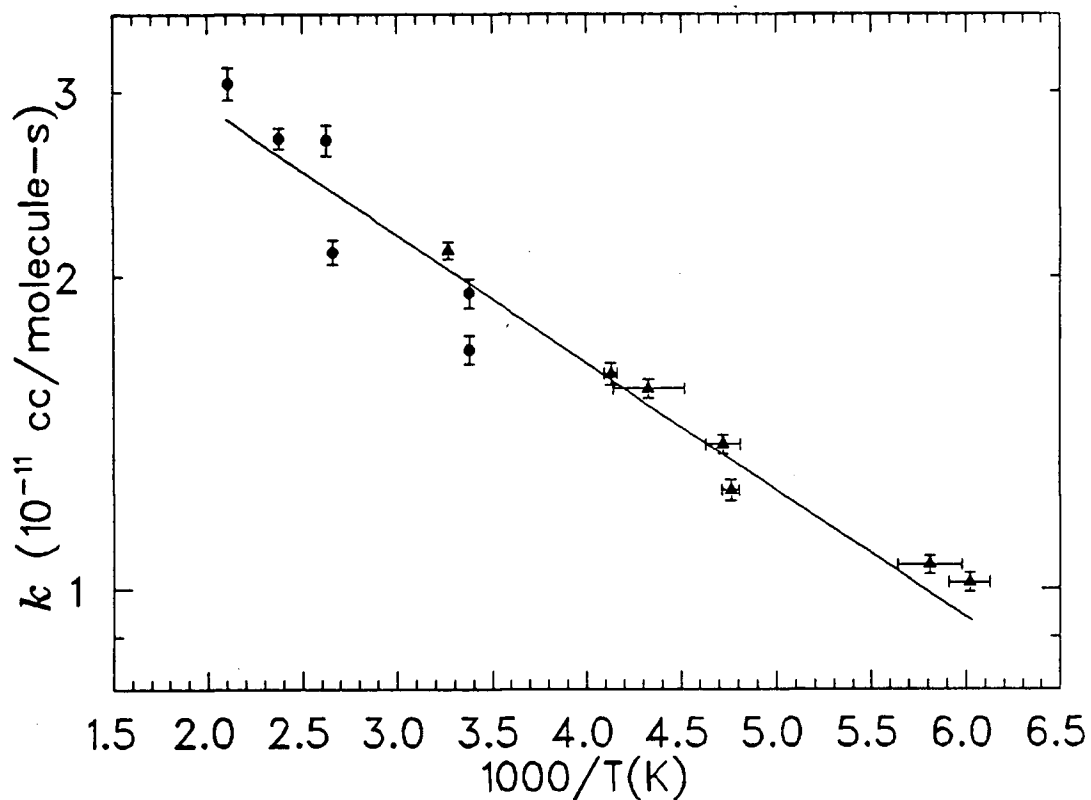


Figure 5.1: Arrhenius plot of $\text{Mu} + \text{HBr}$, fit to $k = Ae^{-E_a/RT}$. Rate constants were measured over the range of 170–480 K. E_a and A were found to be 0.560 ± 0.011 kcal mol $^{-1}$ and $5.101 \pm 0.106 \times 10^{-11}$ cm 3 molecule $^{-1}$ s $^{-1}$, respectively. Data were obtained using a aluminum vessel below room temperature (triangles) and a nickel-plated vessel above room temperature (circles).

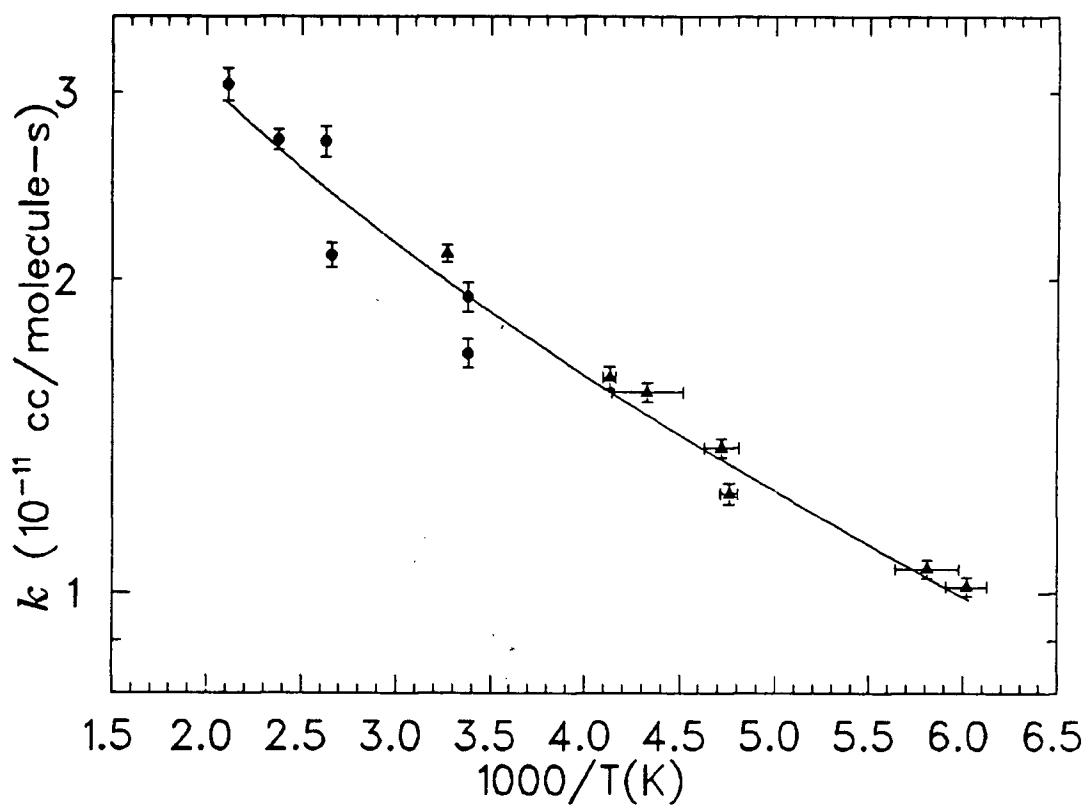


Figure 5.2: Arrhenius plot of $\text{Mu} + \text{HBr}$, fit to $k = BT^{1/2}e^{-E_a/RT}$. Rate constants were measured over the range of 170–480 K. E_a and B were found to be $0.286 \pm 0.014 \text{ kcal mol}^{-1}$ and $0.183 \pm 0.005 \times 10^{-11} \text{ cm}^3 \text{ molecule}^{-1} \text{ s}^{-1}$, respectively. Data were obtained using a aluminum vessel below room temperature (triangles) and a nickel-plated vessel above room temperature (circles).

5.2 Previous Results

5.2.1 Mu + X₂

The muonium atom's role as an isotope of hydrogen, combined with its small mass make it an ideal probe for the study of kinetic isotope effects, manifest in particular by QM tunneling and zero-point energy shifts at the transition state. The pronounced sensitivity of Mu to quantum tunneling was demonstrated very successfully by Gonzalez et al. [9] in their recent paper on muonium reactions with the halogen gases, which provided a major motivation for this thesis as well. In Figure (5.3) the Arrhenius plots for Mu + X₂ (X₂ = F₂, Cl₂, Br₂) are shown. The curvature in the F₂ and Cl₂ plots is clear, indicating that tunneling is the main contributor to the reaction rate at temperatures below ~200 K. In particular, the Mu + F₂ reaction exhibits essentially zero activation energy at the lowest temperatures, showing a transmission coefficient ratio of $\kappa_{\text{Mu}}/\kappa_{\text{H}} = 50$. The trend to both increased reaction rate and decreased tunneling with increasing molecular weight for the halogens in Figure 5.3 can be explained by the change in barrier heights of reaction from 2.30 kcal mol⁻¹ for F₂, decreasing to 1.50 kcal mol⁻¹ for Cl₂, and further decreasing to ~0 kcal mol⁻¹ for Br₂. The latter value could explain not only why no tunneling curvature is seen in the Mu + Br₂ Arrhenius plot, but also why this reaction exhibits a negative E_a (-0.095 ± 0.020 kcal mol⁻¹ [9])

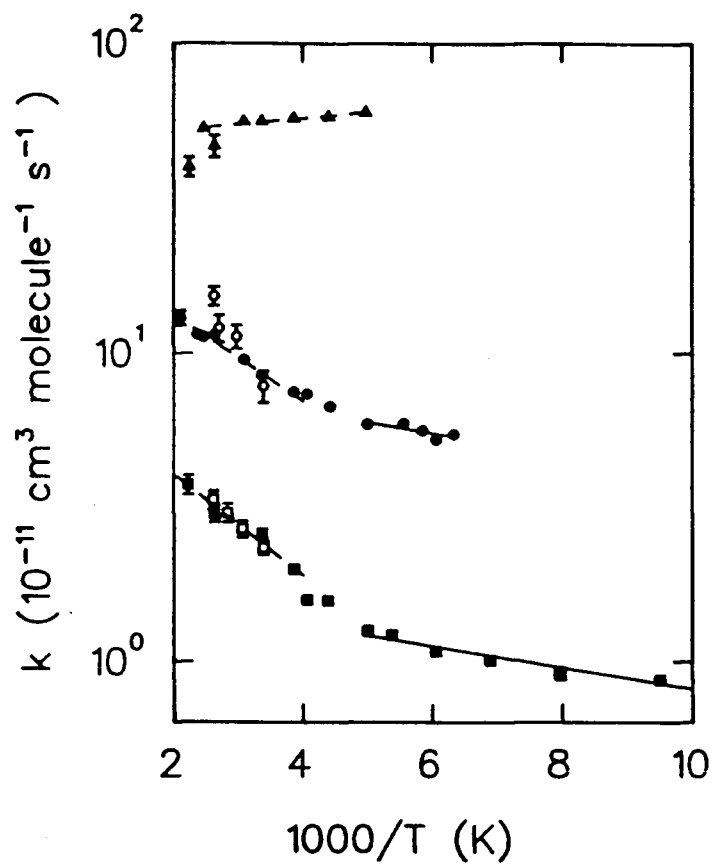


Figure 5.3: Arrhenius plots for $\text{Mu} + \text{X}_2$. The data from Gonzalez et al. [9] is shown with solid points: $\text{Mu} + \text{F}_2$ (squares), $\text{Mu} + \text{Cl}_2$ (circles), and $\text{Mu} + \text{Br}_2$ (triangles). The dashed line segments are Arrhenius fits over $250\text{--}500 \text{ K}$ for $\text{Mu} + \text{F}_2$ and $\text{Mu} + \text{Cl}_2$, and over $200\text{--}400 \text{ K}$ for $\text{Mu} + \text{Br}_2$. The solid line segments represent fits over the range of $100\text{--}200 \text{ K}$ for $\text{Mu} + \text{F}_2$ and $160\text{--}200 \text{ K}$ for $\text{Mu} + \text{Cl}_2$. The open points are previously collected data from the same group.

Because this experiment was so successful in illustrating the importance of tunneling in reactions of muonium with the halogen gases, emphasizing μ SR as a unique and important tool for these types of studies, it was decided that the work could be extended into the series of hydrogen halide gases. The barriers to abstraction reaction for the $\text{H} + \text{HX}$ ($\text{X} = \text{F}, \text{Cl}, \text{I}, \text{Br}$) are on the order of that found for the $\text{Mu} + \text{F}_2$ reaction [9] suggesting that QM tunneling may indeed play an important role in these systems as well.

5.2.2 H(D) + HBr

There have been several theoretical and a few experimental kinetic studies of the reaction of H (and its isotopes) with the hydrogen halides. These have included both the exchange [11, 18, 20, 26, 58, 59] and abstraction [11, 12, 14, 16, 18, 20] reactions, and determination of their state-to-state transitions [14, 21, 26, 60, 61]. In this thesis, since the final product is not identified, the rate constants measured for $\text{Mu} + \text{HBr}$ are the total for both exchange and abstraction, at thermal conditions, so it is important that comparisons with theory and other experiments be done with care.

In the past, in the corresponding studies of the H atom reaction, there has been some controversy over whether abstraction



or exchange



dominates at various temperatures. Most recent experiments [21, 62, 63] have shown the abstraction reaction to be overwhelmingly dominant at room temperature and below. This is explained by the enthalpies of the two reactions; the abstraction reaction is exothermic ($\Delta H = -19.1 \text{ kcal mol}^{-1}$ [14]), while exchange is thermoneutral for $\text{H} + \text{HBr}$, and slightly exothermic for $\text{D} + \text{HBr}$ ($\Delta H = 0.96 \text{ kcal mol}^{-1}$ [63]). In addition, the barrier height, V^\ddagger , of exchange is calculated to be about four times as large as that for abstraction (see Table 5.2). In the case of Mu the exchange is always endothermic ($\Delta H \sim 7 \text{ kcal mol}^{-1}$, see Table 5.5) due to the zero-point energy shift in the product state, so only abstraction can be important over the temperature range of interest in this thesis. Since abstraction appears to be overwhelmingly dominant in H atom kinetics at room temperature and below, and previously determined kinetic data for the total reaction of $\text{H(D)} + \text{HBr}$ is sparse, comparison with abstraction reaction values will also be made.

The PES for the $\text{H(D)} + \text{HBr}$ abstraction reaction has been determined semi-empirically using DIM [23, 59] and LEPS [24], and empirically using the bond-strength-bond-length (BSBL) treatment [19]—the exact PES is unavailable for this system, unlike the $\text{H} + \text{H}_2$ system. Characteristics of the saddle point are given in Table 5.2. The value V^\ddagger for abstraction is relatively low at $\sim 3 \text{ kcal mol}^{-1}$.

As stated by Dunning [18], it has been of great interest to scientists in this field to find a quantitative relationship between heat of reaction,

Table 5.2: Saddle point characteristics of the H₂Br PES.

	Ref	
$V^\ddagger(\text{abstraction, kcal mol}^{-1})$	3.8	18
	2.89	19
$V^\ddagger(\text{exchange, kcal mol}^{-1})$	16.2	18
$R_{\text{H-H}}(\text{equilibrium, \AA})$	0.74	11, 14
$R_{\text{H-Br}}(\text{equilibrium, \AA})$	1.41	20, 11, 14
$R_{\text{H-H}}(\text{saddle pt, \AA})$	1.2	20, 18
$R_{\text{H-Br}}(\text{saddle pt, \AA})$	1.5	20, 18

barrier height, and characteristic bond lengths of the saddle point. From his work done on the reactions of H + HX (X = F, Cl, Br, I) he was able to reach three conclusions concerning the relationship of these properties: 1) Very exothermic reactions are characterised as having small reaction barriers which increase with decreasing exothermicity. 2) Exothermic reactions generally have early saddle points, meaning that the transition state resembles the reactant molecules rather than the product molecules. 3) By combining the above rules it is clear that as the barrier to reaction increases, the saddle point moves to later positions along the PES. Since the classical reaction barrier is mass independent these characteristics of the PES (within the Born-Oppenheimer approximation) are equally applicable to the Mu + HBr reaction.

Providing these findings are correct, the low activation energy of the H(D) + HBr reaction implies an early saddle point on its PES. Furthermore, by comparing the H—H and H—Br bond lengths of the transition state species to their equilibrium values it seems indisputable that the transition state resembles the reactant species and thus constitutes an early reaction barrier on the PES. The H—H bond length is more than 1.5 times larger than its corresponding equilibrium length, whereas the H—Br transition state and equilibrium bond lengths are almost equal (see Table 5.2). It can further be said that since the transition state of a system with an early barrier resembles the reactant molecule, little effect is expected in the zero-point energy of the transition state by replacing H with one of its isotopes (D, T, or Mu). It is thus reasonable to directly compare values of E_a of the H(D) + HBr system with those obtained in this thesis without the need of correcting for varying zero-point energies.

Kinetic data for the H(D) + HBr reaction have been amassed from various experimental and theoretical studies, and is listed in Tables 5.3 and 5.4. The most recent experimental values, obtained by Hepburn and co-workers [16], suggests that the activation energy, of this system is much lower ($< 0.9 \text{ kcal mol}^{-1}$) than previous measurements. As pointed out by Sudhakaran and Raff [20], the molecular beam data [16] seems to be

inconsistent with thermal rate data [11,17], with the latter E_a 's being considerably larger. This has caused some confusion in trying to draw conclusions about the reliability of theoretical calculations. Quasi-classical theory [14,19] supports the higher experimental E_a of 2.570 ± 0.100 kcal mol⁻¹ reported by Endo and Glass [11] for H + HBr. Their value for the D + HBr reaction was 2.130 ± 0.080 kcal mol⁻¹, close to the hydrogen analogue as would be expected for a reaction with an early barrier, but also in the right direction for (small) zero-point energy shifts at the transition state. However, if E_a is indeed small, as found by Hepburn et al. [16] and Steiner [66], its inconsistency with theoretical calculations may be accounted for by assuming that QM tunneling is occurring. It is still unclear as to how much tunneling contributes to the reaction rate of this system, though it is suspected to be relatively low.

Bimolecular rate constants for H(D) + HBr reactions of both experimental and theoretical origin corresponding to the Arrhenius parameters in Table 5.3 are listed in Table 5.4. At 300 K the rate of the H reaction with HBr is faster than that of D, as would be expected from their collision velocities, inversely proportional to the square roots of the masses (recall Equation (3.13)), though the ratio of k_H/k_D is somewhat larger than 1.4. The Endo and Glass data [11] was used for the majority of calculations because it is the most complete set to date for the H(D) + HBr reactions, and it agrees reasonably well with previous experiments done by Takacs and Glass [12], and Steiner [66]. It should be noted that the theoretical

Table 5.3: Kinetic parameters of the H(D) + HBr system

	$E_a(\text{kcal mol}^{-1})$	$\log(A/\text{cm}^3 \text{ mol}^{-1} \text{ s}^{-1})$	Ref
H + HBr			
Experiment	2.570 ± 0.100	14.2 ± 0.1	11
	3.100	14.1	64
	3.700	14.0	64, 65
	0.900		66
	0.9		16
Theory	2.22	13.5	19
	1.74		14
	1.6		1
D + HBr			
Experiment	2.130 ± 0.080	13.6 ± 0.1	11
Theory	0.19	12.8	20
Mu + HBr			
Experiment	0.560 ± 0.011	13.5 ± 0.05	this thesis

Table 5.4: Experimental and theoretical reaction rate constants of the H(D) + HBr system

	k ($\times 10^{-11}$ cm ³ molecule ⁻¹ s ⁻¹)		
	$T = 300$ K	$T = 500$ K	Ref
H + HBr			
Experiment	0.372±0.127	2.08±0.52	11
	0.13	1.02	64
	0.036	0.434	64,65
	0.60±0.1		17
	0.34 ^a		12
	0.281		66
	3.62	0.562	19
Theory	1.94		21
	<hr/>		
D + HBr			
Experiment	0.180 ± 0.044	0.750 ± 0.135	11
	0.41±0.1		17
Theory	0.765	0.866	20
<hr/>			
Mu + HBr			
Experiment	1.99 ± 0.06	2.90 ± 0.11	this thesis

a) measured at 295 K.

calculations, which were obtained for the most part using QCT on LEPS PES's, substantially over-estimate the experimental rate constants of both the H + HBr and D + HBr reactions at 300 K. At 500 K, theoretical predictions are seemingly in much better agreement with experiment, particularly for D + HBr, suggesting that these reactions deviate from classical behaviour as temperature decreases (see Table 5.4).

Lendvay and coworkers [19] constructed a PES for the reverse abstraction reaction ($\text{H}_2 + \text{X} \rightarrow \text{HX} + \text{H}$) using BSBL treatment and calculated the reaction rate coefficients over the temperature range 100–500 K using QCT. They concluded that although the Arrhenius plot of the H + HX abstraction reaction showed slight deviation from linearity, the curvature observed was not significant.

5.3 New Data: Mu + HBr

No theoretical calculation exists for the abstraction rate constant of the Mu + HBr reaction, which was certainly part of the motivation for this thesis. However, because the PES is mass independent it will have the same shape and characteristics, including V^\ddagger , for the Mu + HBr system as was determined semiempirically for the H(D) + HBr system. The activation energy of the Mu abstraction reaction determined from the fit of Equation (3.4) to the data (Figure 5.1) is considerably lower ($0.560 \text{ kcal mol}^{-1}$)

Table 5.5: A comparison of data for the Mu(H,D) + HBr reactions

	HBr	DBr
$\Delta H(\text{H})$ (abstraction, kcal mol ⁻¹)	-19.1	
$\Delta H(\text{H})$ (exchange, kcal mol ⁻¹)	0	0.96
$\Delta H(\text{Mu})$ (abstraction, kcal mol ⁻¹)	-9.8	-9.7
$\Delta H(\text{Mu})$ (exchange, kcal mol ⁻¹)	7.1	7.0
$E_a(\text{Mu})$ (kcal mol ⁻¹)	0.560	
$E_a(\text{H})^a$ (kcal mol ⁻¹)	2.57	
$E_a(\text{D})^a$ (kcal mol ⁻¹)	2.13	
KIE ₃₀₀ (Mu/H) ^a	5.3	
KIE ₃₀₀ (Mu/H) ^b	3.3	
KIE ₃₀₀ (H/D) ^a	2.1	2.2
KIE ₃₀₀ (H/D) ^b	1.5	
KIE ₅₀₀ (Mu/H) ^a	1.4	
$\kappa_{\text{Mu}}/\kappa_{\text{H}}(300 \text{ K})^a$	1.8	
$\kappa_{\text{Mu}}/\kappa_{\text{H}}(300 \text{ K})^b$	1.1	
$\kappa_{\text{H}}/\kappa_{\text{D}}(300 \text{ K})^a$	1.5	
$\kappa_{\text{H}}/\kappa_{\text{D}}(300 \text{ K})^b$	1.1	
$(m_{\text{D}}^*)^{1/2}/(m_{\text{H}}^*)^{1/2}$	1.4	
$(m_{\text{H}}^*)^{1/2}/(m_{\text{Mu}}^*)^{1/2}$	2.9	

a) H/D data from Endo and Glass [11].

b) H/D data from Husain and Slater [17].

than even the lowest E_a determined for the equivalent H reaction by Hepburn et al. (0.900 kcal mol⁻¹) [16]. Since this value is so low, and the Mu + HBr reaction is exothermic, we can again assume an early reaction barrier according to the findings of Dunning [18] discussed in the previous section. The transition state for this specific case resembles the reactant species such that the zero-point energy of the transition state will be largely the same for each isotopic variant of the H + HBr reaction. The extremely low E_a observed in the Mu reaction relative to both H and D strongly suggests that QM tunnelling is occurring.

In contrast to the F₂ and Cl₂ data in Figure 5.3, where pronounced curvature is seen in the experimental Arrhenius plots at the lowest temperatures, the Arrhenius plot for Mu + HBr shown in Figure (5.1) exhibits a straight line dependence over a similar temperature range, seemingly disputing the evidence for tunneling seen in the E_a value. If QM tunneling dominates the reaction kinetics, one expects to see a flattening out in the curve as $T \rightarrow 0$, in accordance with Equation (3.30). In some cases for exothermic reactions with high enough energy barriers, the E_a actually approaches zero below a certain temperature, a condition known as Wigner threshold tunneling. Below this temperature tunneling dominates completely over classical behaviour as the mechanism with which the reactants reach the product valley of the PES. This effect has been seen for the first time in the gas phase in the aforementioned Mu + F₂ reaction data (Figure 5.3) [9].

Whether or not QM tunneling dominates at the temperatures of a given experiment can be answered by examining the condition under which the Wigner law holds true [53]. As previously discussed, the Wigner law predicts that for a highly exothermic reaction, at low enough temperature, the rate constant obeys the proportionality given in Equation (3.30) (i.e., the rate constant becomes temperature independent and $E_a = 0$). The Wigner law is expected to be obeyed if the ratio of the de Broglie wavelength, λ , to barrier thickness, t , is much greater than unity. By expressing λ in terms of the translational energy, E , which in turn is equal to kT , an upper limit on the temperature at which the Wigner law applies is obtained.

$$T \ll \frac{h^2}{2\mu kt^2} \quad (5.4)$$

Using a barrier thickness of $\sim 3 \text{ \AA}$, which is typical for $\text{H}(\text{Mu}) + \text{F}_2$ [70] or $\text{H}(\text{Mu}) + \text{HBr}$ [67], the temperature below which tunneling should dominate the Mu kinetics is $\sim 1000 \text{ K}$. This can be compared with $\sim 100 \text{ K}$ for the corresponding H atom reactions. The Arrhenius plot for $\text{Mu} + \text{HBr}$ extends well below 1000 K confirming that the temperature region where QM tunneling should dominate is well represented in this experiment; the situation is similar for $\text{Mu} + \text{F}_2$ (Figure 5.3). However, it is clear from a comparison of these figures that tunneling is relatively unimportant in the case of $\text{Mu} + \text{HBr}$, in marked contrast to the F_2 case. In retrospect, this may not be surprising in view of the fact that the $\text{Mu} + \text{HBr} \rightarrow \text{MuH} + \text{Br}$ reaction is an order of magnitude less exothermic than $\text{Mu} + \text{F}_2$. The Wigner law may be expected to be less valid at this more conservative

exothermicity.

Nevertheless, the rate constant of $\text{Mu} + \text{HBr}$ at 300 K (see Table 5.4) is considerably higher than values determined experimentally for the analogous H and D reactions. The KIE's at 300 and 500 K are listed in Table 5.5. The $\text{KIE}_{300}(\text{H}/\text{D})$ is 2.1 or 1.5 according to Endo and Glass [22], or Husain and Slater [34], respectively. Comparison of these values with the trivial mass dependence given by collision theory, $(m)^{-1/2}$, reveals the extent of QM effects taking place in the reaction. This ratio is 1.4 for $(m_{\text{D}}^*)^{1/2}/(m_{\text{H}}^*)^{1/2}$, very close to the Husain and Slater data, and slightly lower than that of Endo and Glass, though not appreciably. The extent of tunneling reflected by these values is low, as are zero-point energy shifts at the transition state, noted earlier.

$\text{KIE}_{300}(\text{Mu}/\text{D})$ is 5.3 or 3.32 calculated from data given by Endo and Glass, or Husain and Slater, respectively. Comparing these numbers to the classical value of 2.9, the experimental ratios are larger with the Husain and Slater data again giving a more conservative estimate of the non-classical contribution to the $\text{Mu} + \text{HBr}$ rate constant. On average these give a ratio of transmission coefficients $\kappa_{\text{Mu}}/\kappa_{\text{H}} \sim 1.5$ (Table 5.5). Oddly, at 500 K the value of $\text{KIE}_{500}(\text{Mu}/\text{H})$ is less than the classical value based on the data of Endo and Glass. This could simply reflect experimental error, or may be an indication of an unusually long range attractive potential.

All of the transmission coefficient ratios for the $\text{H}(\text{D},\text{Mu}) + \text{HBr}$ reactions given in Table 5.5 are greater than unity, though only by a small

amount. As noted, on average $\kappa_{\text{Mu}}/\kappa_{\text{H}}$ at 300 K is 1.5. Even the value of 1.8 calculated using the data of Endo and Glass indicates a very small contribution of QM tunneling (compare this with $\kappa_{\text{Mu}}/\kappa_{\text{H}} = 5.7$ at 300 K for $\text{Mu} + \text{F}_2$).

The preexponential factor can be calculated due purely to classical contributions using hard sphere collision theory. If we equate Equations (3.4) and (3.14) (i.e. $E_a = E_0$) the A factor is expressed by

$$A = d^2 \left(\frac{8\pi kT}{\mu} \right)^{1/2} \quad (5.5)$$

where d is the physical cross section represented by the sum of the radii of Mu and HBr. Assuming this to be a hard sphere collision is equivalent to saying that the activation energy is zero, which in the case of $\text{Mu} + \text{HBr}$ is not unreasonable since the experimental value of E_a is so low. A calculation of this nature often gives reasonable preexponential values for exothermic reactions involving atom-molecule collisions. To complete the calculation, the reduced mass and classical cross section of the $\text{Mu} + \text{HBr}$ system must be known. These can be determined as follows:

$$\begin{aligned} \mu &= \frac{m_{\text{Mu}}m_{\text{HBr}}}{m_{\text{Mu}} + m_{\text{HBr}}} \\ &= 0.1138 \text{ g mol}^{-1} \end{aligned} \quad (5.6)$$

$$= 1.89 \times 10^{-28} \text{ kg molecule}^{-1} \quad (5.7)$$

Since the Mu atom ‘bonds’ with the H atom in the HBr abstraction reaction, the effective cross section of collision can be calculated using the radii of

Mu and H taken from Table 2.1. Thus,

$$\begin{aligned}d^2 &= (r_{\text{Mu}} + r_{\text{H}})^2 \\&= (0.5315 + 0.5292)^2 \text{ \AA}^2 \\&= 1.1251 \text{ \AA}^2 \\&= 1.1251 \times 10^{-20} \text{ m}^2\end{aligned}\tag{5.8}$$

Substituting these values into the equation for A we get

$$\begin{aligned}A &= 1.1251 \times 10^{-20} \left(\frac{8\pi(1.3805 \times 10^{-23})(300)}{1.89 \times 10^{-28}} \right)^{1/2} \\&= 2.64 \times 10^{-10} \text{ cm}^3 \text{ molecule}^{-1} \text{ s}^{-1}\end{aligned}\tag{5.9}$$

This is reasonably close to the value obtained in this experiment ($(0.5101 \pm 0.0106) \times 10^{-10} \text{ cm}^3 \text{ molecule}^{-1} \text{ s}^{-1}$) indicating that the behaviour of the Mu + HBr reaction can be successfully modelled by simple hard sphere collision theory at the temperatures exceeding 170 K, thus further confirming the relative lack of tunneling characteristics seen in the Arrhenius plot (Figure 5.1).

Chapter 6

Conclusion

The kinetic rate constants of $\text{Mu} + \text{HBr}$ were measured over a temperature range of 170–480 K. It was found that the activation energy of this reaction was lower ($0.560 \pm 0.011 \text{ kcal mol}^{-1}$) than expected, opening the possibility that the reaction is dominated by quantum tunneling. However, transmission coefficient ratios, $\kappa_{\text{Mu}}/\kappa_{\text{H}}$, were only slightly greater than unity indicating that the $\text{Mu} + \text{HBr}$ reaction's behaviour is mostly classically, even at low temperatures. More evidence for this was provided by the reasonable agreement of a simple collision theory calculation with experiment. This, coupled with the low exothermicity of the reaction, means QM tunneling is relatively unimportant. This conclusion was supported by the Arrhenius plot which lacked the typical curvature and leveling off at low temperatures, a distinguishing feature in reactions where tunneling is significant. Comparing the present $\text{Mu} + \text{HBr}$ data with the $\text{Mu} + \text{F}_2$ and $\text{Mu} + \text{Br}_2$ data measured in a previous experiment at TRIUMF [9], it was found that the $\text{Mu} + \text{HBr}$ reaction more closely resembles the Br_2 data in

that both have small, or even negative (Br_2) E_a 's. It is believed that the negative E_a of $\text{Mu} + \text{Br}_2$ is indicative of a highly attractive and particularly long range PES, which is consistent with the energy dependence of $\sigma(E)$ measured for $\text{H} + \text{Br}_2$ by molecular beam experiments [68]. This type of behaviour is typically seen in ion-molecule (capture) reactions [69] and is characterized by $E_a \leq 0$ and $k(T) \sim T^0$, the same condition observed in Wigner threshold tunneling for an exothermic reaction. Reactions exhibiting this behaviour tend to be highly exothermic, as is the case for $\text{H} + \text{Br}_2$. However, this is not so for $\text{Mu} + \text{HBr}$ whose abstraction reaction is exothermic by only $9.8 \text{ kcal mol}^{-1}$. Despite this, the barrier to reaction of $\text{Mu} + \text{HBr}$ was found to be extremely low, suggesting that either the theoretical calculations over-estimate its value, or the barrier is positioned somewhat later than previously thought.

Bibliography

- [1] Garwin, R.L., Lederman, L.M., Weinrich, M., *Physical Rev.*, (1957) **105**, 1415.
- [2] Brewer, J.H., Crowe, K.M. in "Annual Review of Nuclear and Particle Science", vol.28, p.239, J.D. Jackson, H.E. Gove, R.F. Schwitters, Eds., Annual Reviews Inc., Palo Alto, California, USA, 1978.
- [3] Garner, D.M., Ph.D. Thesis, University of British Columbia, 1979 (unpublished).
- [4] Walker, D.C., "Muon and Muonium Chemistry", Cambridge University Press, Cambridge, 1983.
- [5] Swanson, R.A., *Physical Rev.*, (1958) **112**, 580.
- [6] Schatz, G.C., *Chem. Rev.*, (1987) **87**, 81.
- [7] Bodenstein, M., Lind, S.C., *Z. Phys. Chem.*, (1906) **57**, 168.
- [8] Bodenstein, M., Lütkemeyer, H., *Z. Phys. Chem.*, (1924) **114**, 208.
- [9] Gonzalez, A.C., Reid, I.D., Garner, D.M., Senba, M., Fleming, D.G., Arseneau, D.J., Kempton, J.R., *J. Chem. Phys.*, (1989) **91**, 6164.
- [10] Eyring, H., Polanyi, M., *Z. Phys. Chem.*, (1931) **B12**, 279.
- [11] Endo, H., Glass, G.P., *J. Phys. Chem.*, (1976) **80**, 1519.
- [12] Takacs, G.A., Truhlar, D.G., *J. Phys. Chem.*, (1973) **77**, 1060.
- [13] Zhang, Y.C., Zhang, J.Z.H., Kouri, D.J., Haug, K., Schwenke, D.W., Truhlar, D.G., *Phys. Rev. Lett.*, (1988) **60**, 2367.
- [14] Aker, P.M., Valentini, J.J., *Israel J. Chem.*, (1990) **30**, 157.

- [15] McDonald, J.D., Herschbach, D.R., *J. Chem. Phys.*, (1975) **62**, 4740.
- [16] Hepburn, J.W., Klimek, D., Liu, K., Macdonald, R.G., Northrup, F.J., Polanyi, J.C., *J. Chem. Phys.*, (1981) **74**, 6226.
- [17] Husain, D., Slater, N.H., *J. Chem. Soc. Faraday Trans. II*, (1980) **76**, 276.
- [18] Dunning, Jr., T.H., *J. Phys. Chem.*, (1984) **88**, 2469.
- [19] Lendvay, G., Laszlo, B., Berces, T., *Chem. Phys. Lett.*, (1987) **137**, 175.
- [20] Sudhakaran, M.P., Raff, L.M., *Chem. Phys.*, (1985) **95**, 165.
- [21] White, J.M., Thompson, D.L., *J. Chem. Phys.*, (1974) **61**, 719.
- [22] Porter, R.N., Sims, L.B., Thompson, D.L., Raff, L.M., *J. Chem. Phys.*, (1973) **58**, 2855.
- [23] Ellison, F.O., Patel, J.C., *J. Amer. Chem. Soc.*, (1964) **86**, 2115.
- [24] Sato, S., *J. Chem. Phys.*, (1955) **23**, 2465.
- [25] Clary, D.C., *Chem. Phys.*, (1982) **71**, 117.
- [26] Aker, P.M., Germann, G.J., Tabor, K.D., Valentini, J.J., *J. Chem. Phys.*, (1989) **90**, 4809.
- [27] Street, J.C., Stevenson, E.C., *Physical Rev.*, (1937) **52**, 1003.
- [28] Anderson, C.D., Neddermeyer, S., *Physical Rev.*, (1938) **54**, 88.
- [29] Arseneau, D.J., M.Sc. Thesis, University of British Columbia, 1984 (unpublished).
- [30] Fleming, D.G., Garner, D.M. in "Positronium and Muonium Chemistry", p.279, American Chemical Society, Washington, DC, 1979.
- [31] Weissenberg, A.O., "Muons", North-Holland Publishing Co., Amsterdam, 1967.

- [32] Hughes, V.W., McColm, D.W., Ziock, K., Prepost, R., *Physical Rev. A*, (1970) **1**, 595.
- [33] Burton, W.B. in "Galactic and Extragalactic Radio Astronomy", p.95, G.L. Verschuur, K.I. Kellermann, Eds., Springer-Verlag, New York, 1974.
- [34] van't Hoff, J.H., "Etudes de Dynamique Chimique", Muller, Amsterdam, 1884.
- [35] Arrhenius, S., *Z. Phys. Chem.*, (1889) **4**, 226.
- [36] Laidler, K.J., "Chemical Kinetics", Harper & Row, New York, 1987.
- [37] Schatz, G.C., *J. Chem. Phys.*, (1985) **83**, 3441.
- [38] Liu, B., Siegbahn, P., *J. Chem. Phys.*, (1978) **68**, 2457.
- [39] Reid, I.D., Garner, D.M., Lee, L.Y., Senba, M., Arseneau, D.J., Fleming, D.G., *J. Chem. Phys.*, (1987) **86**, 5578.
- [40] Laidler, K.J., King, M.C., *J. Phys. Chem.*, (1983) **87**, 2657.
- [41] Sato, S., *J. Chem. Phys.*, (1955) **23**, 592.
- [42] Hirst, D.M., "Potential Energy Surfaces: molecular structure and reaction dynamics", p.115, Taylor and Francis, London, 1985.
- [43] Eyring, H., *J. Chem. Phys.*, (1935) **3**, 107.
- [44] Evans, M.G., Polanyi, M., *Trans. Far. Soc.*, (1935) **31**, 875.
- [45] Truhlar, D.G., Hase, W.L., Hynes, J.T., *J. Phys. Chem.*, (1983) **87**, 2664.
- [46] Johnston, H.S., Rapp, D., *J. Amer. Chem. Soc.*, (1961) **83**, 1.
- [47] Truhlar, D.G., Gordon, M.S., *Science*, (1990) **249**, 491.
- [48] Truhlar, D.G., Garrett, B.C., *Acc. Chem. Res.* (1980) **13**, 440.
- [49] Truhlar, D.G., Garrett, B.C., *Ann. Rev. Phys. Chem.* (1984) **35**, 159.

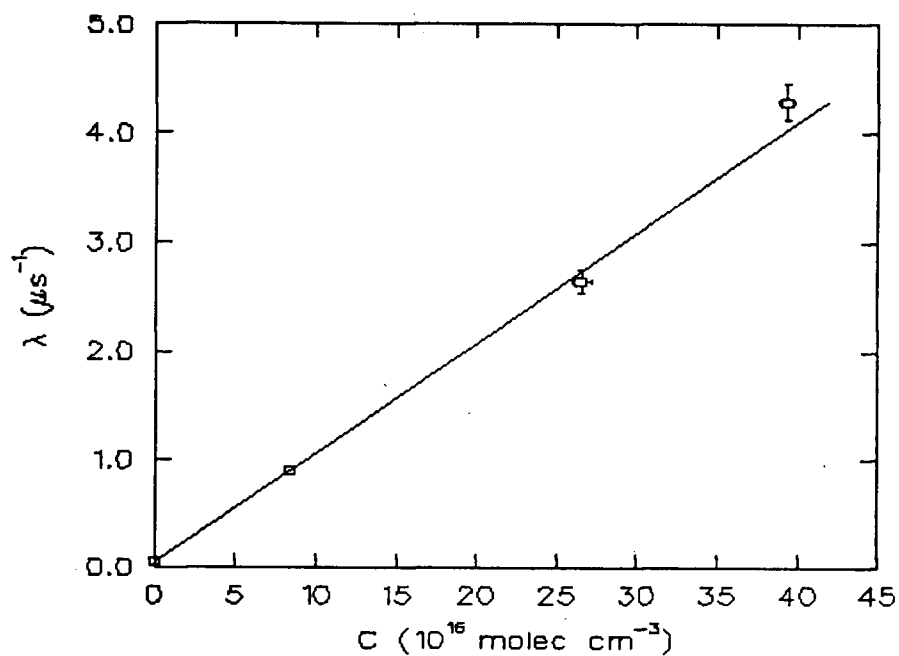
- [50] Truhlar, D.G., Isaacson, A.D., Skodje, R.T., Garrett, B.C., *J. Phys. Chem.* (1982) **86**, 2252.
- [51] Skodje, R.T., Truhlar, D.G., Garrett, B.C., *J. Phys. Chem.*, (1981) **85**, 3019.
- [52] Garrett, B.C., Truhlar, D.G., Grev, R.S., Magnuson, A.W., *J. Phys. Chem.*, (1980) **84**, 1730.
- [53] Takayanagi, T., Masaki, N., Nakamura, K., Okamoto, M., Sato, S., Schatz, G.C., *J. Chem. Phys.*, (1987) **86**, 6133.
- [54] Senba, M., Arseneau, D.J., Gonzalez, A.C., Kempton, J.R., Pan, J.J., Tempelmann, A., Fleming, D.G., *Hyper. Inter.* (in press).
- [55] James, F., Roos, M., MINUIT, CERN Computer 7600 Interim Program Library, (1971).
- [56] Arseneau, D.J., Ph.D. Thesis, University of British Columbia, (in progress).
- [57] Senba, M., private communication.
- [58] Lynch, G.C., Truhlar, D.G., Garrett, B.C., *J. Chem. Phys.*, (1989) **90**, 3102.
- [59] Last, I., Baer, M., *J. Chem. Phys.*, (1984) **80**, 3246.
- [60] Clary, D.C., *J. Chem. Phys.*, (1985) **83**, 1685.
- [61] Clary, D.C., *Chem. Phys.*, (1983) **81**, 379.
- [62] Su, H.Y., White, J.M., Raff, L.M., Thompson, D.L., *J. Chem. Phys.*, (1975) **62**, 1435.
- [63] Persky, A., Kuppermann, A., *J. Chem. Phys.*, (1974) **61**, 5035.
- [64] Fass, R.A., *J. Phys. Chem.*, (1970) **74**, 984.
- [65] Cooley, S.D., Anderson, R.C., *Ind. Eng. Chem.*, (1952) **44**, 1402.
- [66] Steiner, G.B., *Proc. Roy. Soc. Ser. A*, (1939) **173**, 531.

- [67] Baer, M., Last, I. in "Potential Energy Surfaces and Dynamic Calculations", D.G. Truhlar, Ed., Plenum Press, New York, 1981.
- [68] Hepburn, J.W., Klimek, D., Liu, K., Polanyi, J.C., Wallace, Jr., S.C., *J. Chem. Phys.*, (1978) **69**, 4311.
- [69] Arseneau, D.J., Fleming, D.G., Senba, M., Reid, I.D., Garner, D.M., *J. Chem. Phys.*, (1988) **66**, 2018.
- [70] Steckler, R., Truhlar, D.G., Garrett, B.C., *Int. J. Quantum Chem. Symp.*, (1986) **20**, 495.

Appendix A

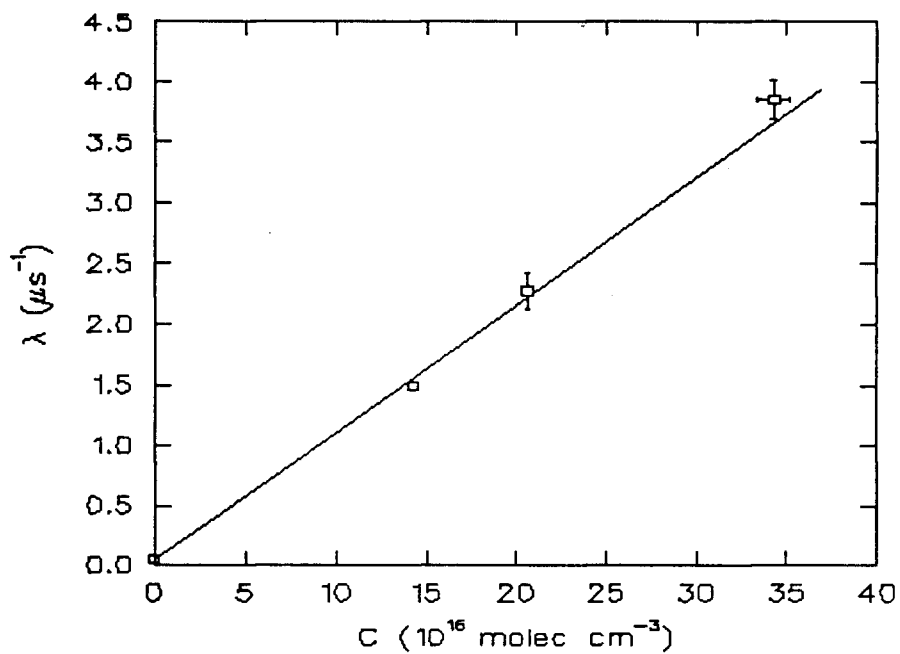
Data

The following pages show relaxation rates versus HBr concentration at various temperatures. The straight line on each graph shows the best fit to Equation (5.1). The slope, k , is given at the bottom of each table.

Figure A.1: HBr in N_2 , 166 ± 3 K.

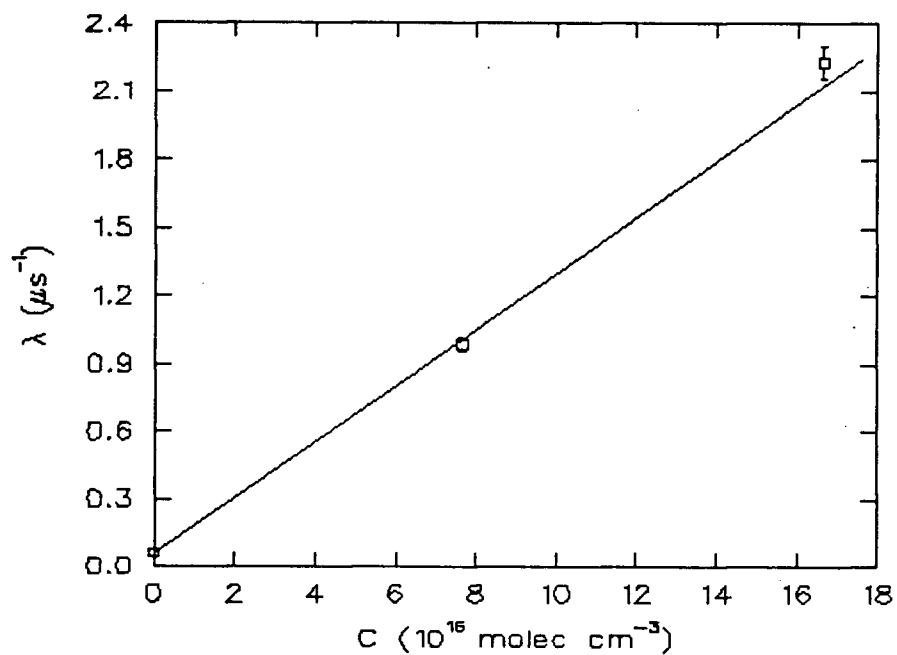
[HBr] 10^{16} molec cm^{-3}	λ μs^{-1}
0.00 ± 0.00	0.0513 ± 0.0029
26.51 ± 0.62	2.64 ± 0.11
8.400 ± 0.020	0.894 ± 0.028
39.31 ± 0.50	4.29 ± 0.16

$$k = (1.015 \pm 0.021) \times 10^{-11} \text{ cm}^3 \text{ molecule}^{-1} \text{ s}^{-1}.$$

Figure A.2: HBr in N₂, 172 ± 5 K.

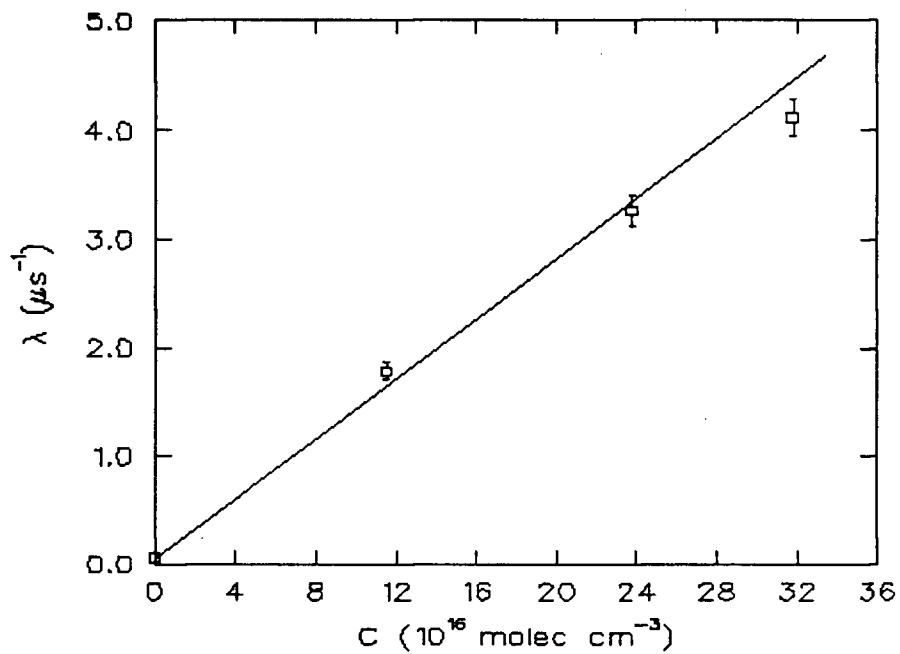
[HBr]	λ
$10^{16} \text{ molec cm}^{-3}$	μs^{-1}
0.00 ± 0.00	0.0513 ± 0.0029
14.26 ± 0.10	1.488 ± 0.043
34.24 ± 0.84	3.86 ± 0.16
20.620 ± 0.050	2.28 ± 0.15

$$k = (1.055 \pm 0.021) \times 10^{-11} \text{ cm}^3 \text{ molecule}^{-1} \text{ s}^{-1}.$$

Figure A.3: HBr in N₂, 210 ± 2 K.

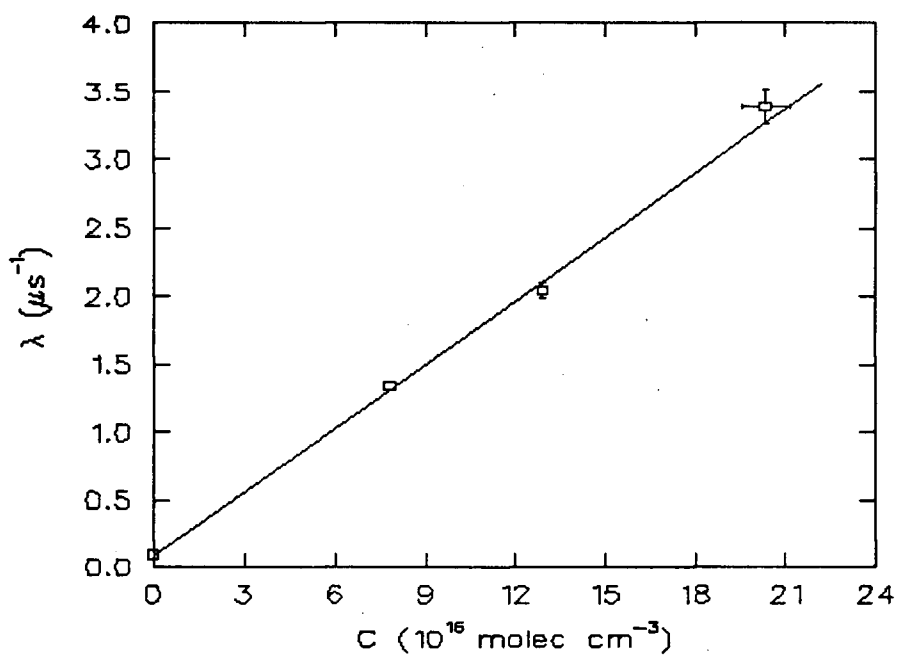
[HBr] 10 ¹⁶ molec cm ⁻³	λ μs ⁻¹
0.00 ± 0.00	0.0599 ± 0.0039
16.650 ± 0.070	2.230 ± 0.072
7.650 ± 0.020	0.983 ± 0.028

$$k = (1.247 \pm 0.028) \times 10^{-11} \text{ cm}^3 \text{ molecule}^{-1} \text{ s}^{-1}.$$

Figure A.4: HBr in N₂, 212 ± 4 K.

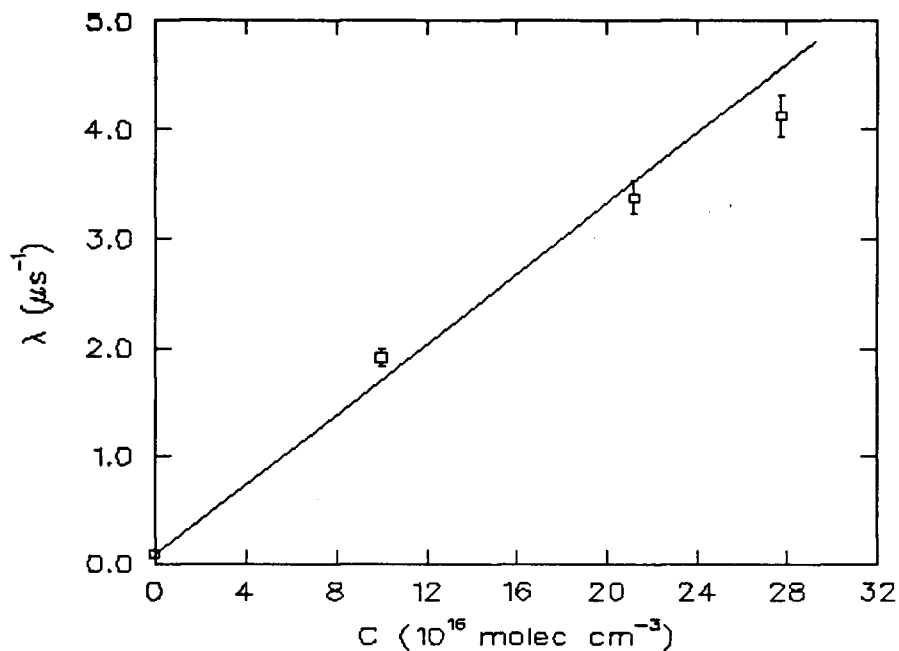
[HBr] 10 ¹⁶ molec cm ⁻³	λ μs ⁻¹
0.00 ± 0.00	0.0599 ± 0.0039
11.53 ± 0.12	1.785 ± 0.076
23.760 ± 0.050	3.26 ± 0.15
31.760 ± 0.020	4.12 ± 0.17

$$k = (1.381 \pm 0.028) \times 10^{-11} \text{ cm}^3 \text{ molecule}^{-1} \text{ s}^{-1}.$$

Figure A.5: HBr in N₂, 231 ± 10 K.

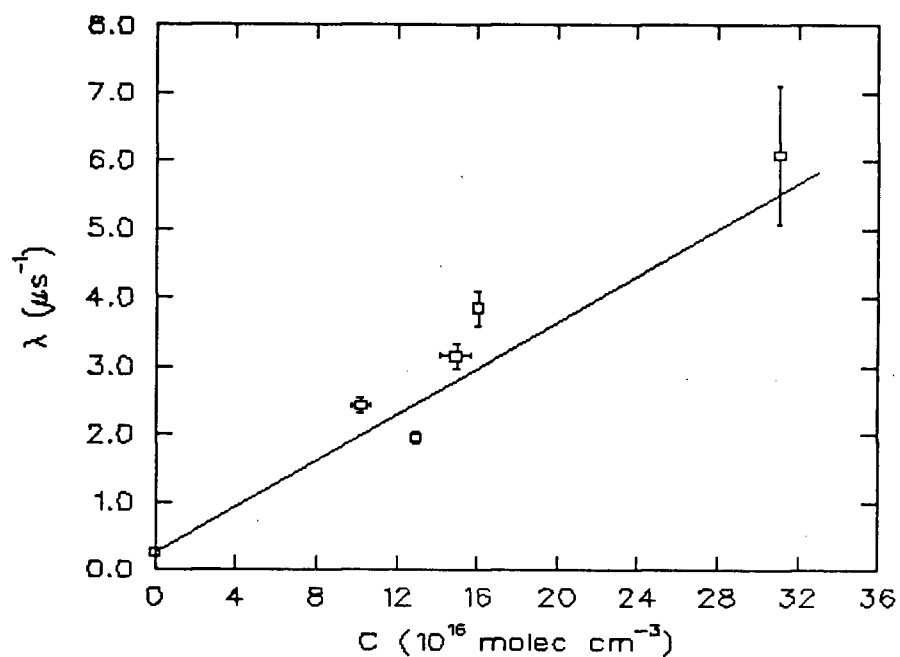
[HBr] 10 ¹⁶ molec cm ⁻³	λ μs ⁻¹
0.00 ± 0.00	0.0885 ± 0.0028
7.850 ± 0.020	1.334 ± 0.040
20.33 ± 0.80	3.39 ± 0.12
12.920 ± 0.070	2.046 ± 0.061

$$k = (1.563 \pm 0.032) \times 10^{-11} \text{ cm}^3 \text{ molecule}^{-1} \text{ s}^{-1}.$$

Figure A.6: HBr in N₂, 242 ± 2 K.

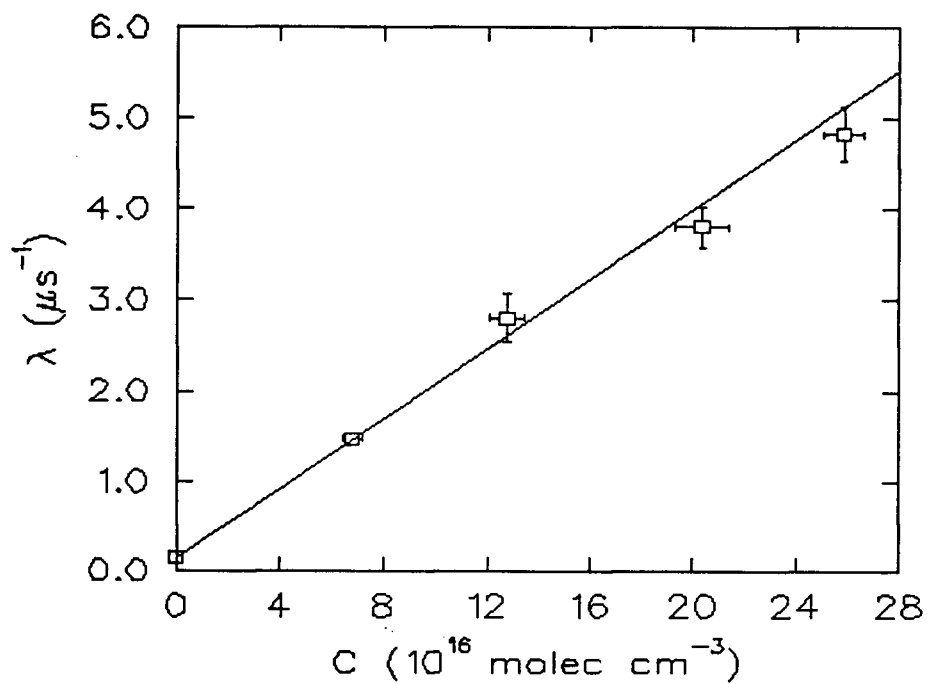
[HBr] 10 ¹⁶ molec cm ⁻³	λ μs ⁻¹
0.00 ± 0.00	0.0885 ± 0.0028
10.04 ± 0.10	1.914 ± 0.075
21.22 ± 0.30	3.37 ± 0.15
27.71 ± 0.17	4.13 ± 0.19

$$k = (1.615 \pm 0.040) \times 10^{-11} \text{ cm}^3 \text{ molecule}^{-1} \text{ s}^{-1}.$$

Figure A.7: HBr in N₂, 296 ± 1 K.

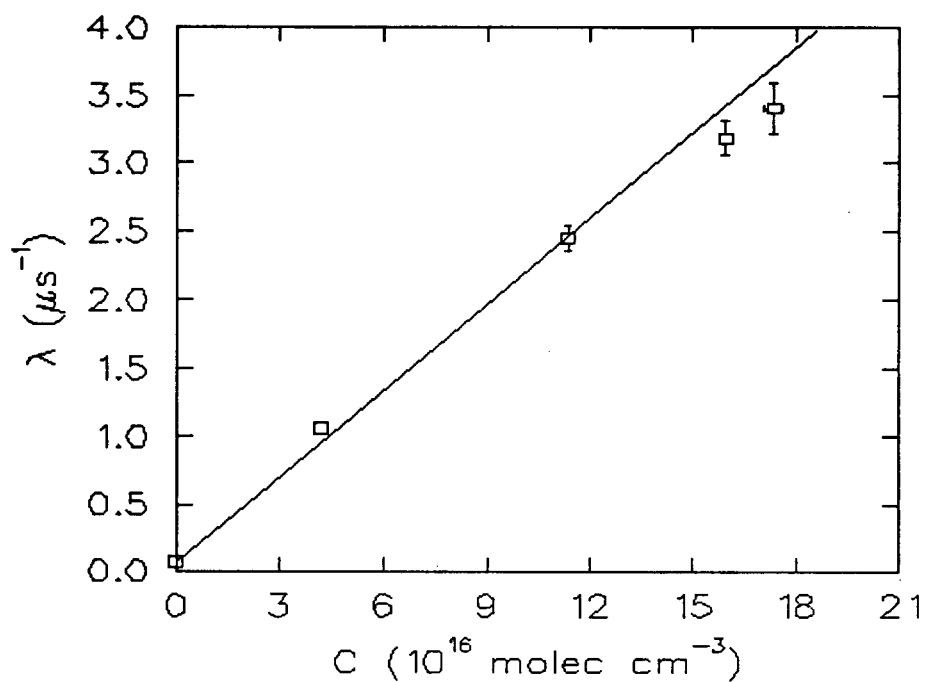
[HBr] 10 ¹⁶ molec cm ⁻³	λ μs ⁻¹
0.00 ± 0.00	0.2485 ± 0.0091
12.94 ± 0.31	1.952 ± 0.088
31.05 ± 0.33	6.1 ± 1.0
14.95 ± 0.74	3.15 ± 0.18
10.19 ± 0.47	2.42 ± 0.12
16.020 ± 0.080	3.85 ± 0.25

$$k = (1.702 \pm 0.054) \times 10^{-11} \text{ cm}^3 \text{ molecule}^{-1} \text{ s}^{-1}.$$

Figure A.8: HBr in N₂, 296 ± 1 K.

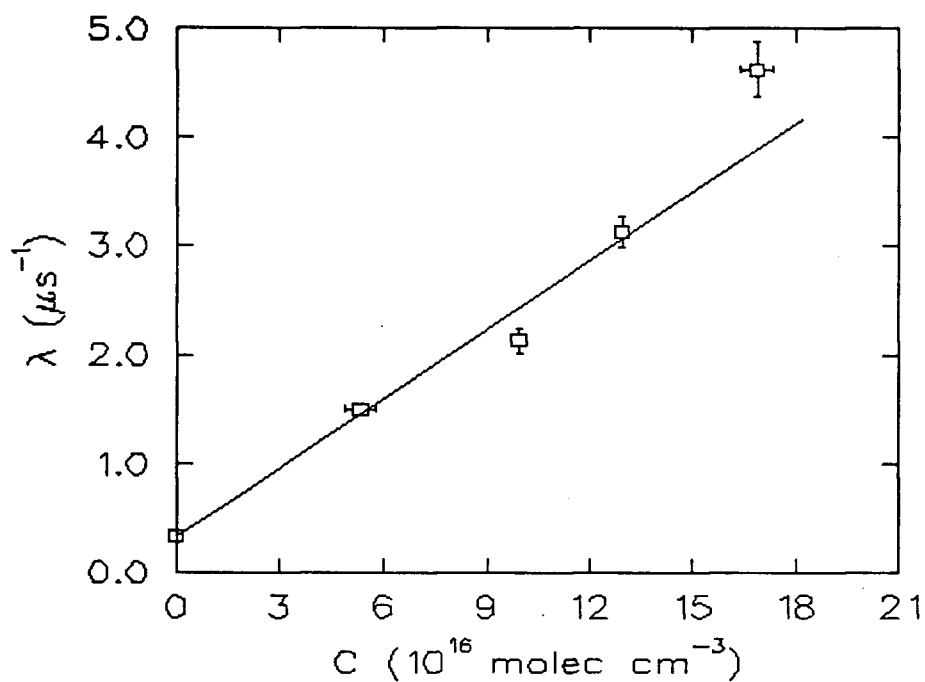
[HBr] 10 ¹⁶ molec cm ⁻³	λ μs ⁻¹
0.00 ± 0.00	0.1434 ± 0.0069
6.81 ± 0.35	1.466 ± 0.056
12.80 ± 0.64	2.80 ± 0.27
20.3 ± 1.0	3.80 ± 0.21
25.82 ± 0.80	4.83 ± 0.30

$$k = (1.926 \pm 0.061) \times 10^{-11} \text{ cm}^3 \text{ molecule}^{-1} \text{ s}^{-1}.$$

Figure A.9: HBr in N₂, 306 ± 2 K.

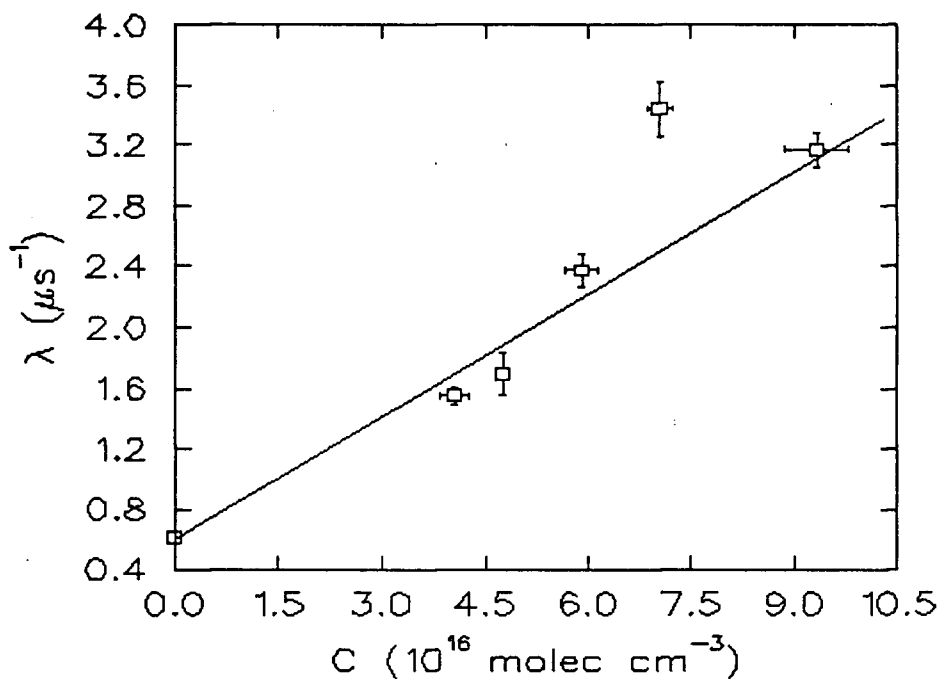
[HBr] 10 ¹⁶ molec cm ⁻³	λ μs ⁻¹
0.00 ± 0.00	0.0640 ± 0.0038
4.170 ± 0.050	1.054 ± 0.028
11.38 ± 0.12	2.449 ± 0.091
17.34 ± 0.30	3.41 ± 0.19
15.950 ± 0.020	3.19 ± 0.13

$$k = (2.115 \pm 0.040) \times 10^{-11} \text{ cm}^3 \text{ molecule}^{-1} \text{ s}^{-1}.$$

Figure A.10: HBr in N₂, 376 ± 1 K.

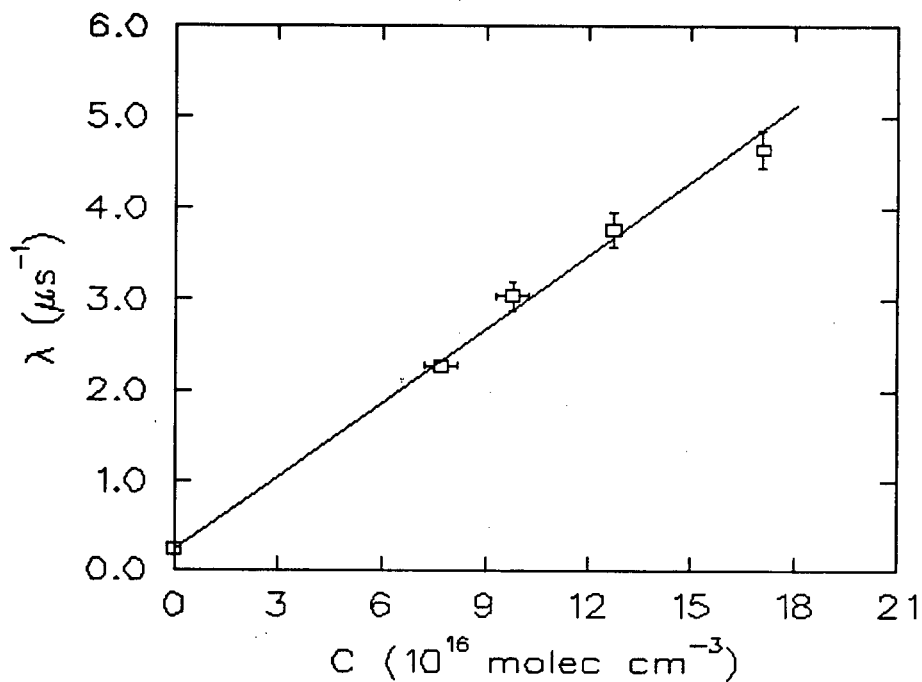
[HBr]	λ
$10^{16} \text{ molec cm}^{-3}$	μs^{-1}
0.00 ± 0.00	0.328 ± 0.011
16.84 ± 0.47	4.63 ± 0.26
9.930 ± 0.020	2.13 ± 0.12
5.33 ± 0.45	1.501 ± 0.056
12.940 ± 0.080	3.12 ± 0.14

$$k = (2.110 \pm 0.054) \times 10^{-11} \text{ cm}^3 \text{ molecule}^{-1} \text{ s}^{-1}.$$

Figure A.11: HBr in N₂, 380 ± 1 K.

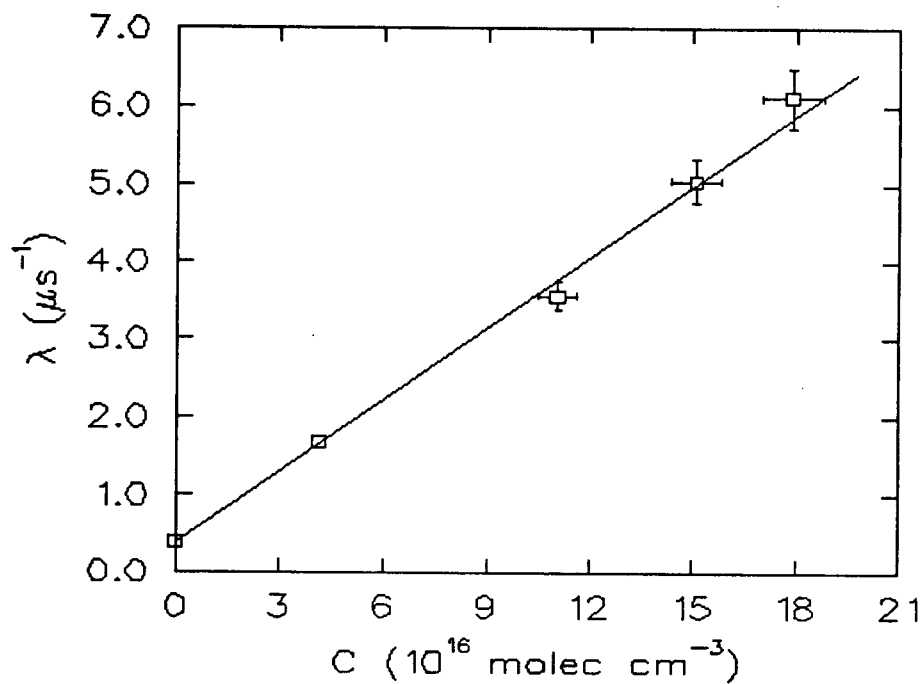
[HBr]	λ
10 ¹⁶ molec cm ⁻³	μs ⁻¹
0.00 ± 0.00	0.613 ± 0.024
9.33 ± 0.47	3.17 ± 0.12
7.05 ± 0.18	3.45 ± 0.18
4.06 ± 0.21	1.548 ± 0.058
4.760 ± 0.060	1.70 ± 0.14
5.91 ± 0.23	2.38 ± 0.11

$$k = (2.699 \pm 0.091) \times 10^{-11} \text{ cm}^3 \text{ molecule}^{-1} \text{ s}^{-1}.$$

Figure A.12: HBr in N₂, 421 ± 2 K.

[HBr] 10 ¹⁶ molec cm ⁻³	λ μs ⁻¹
0.00 ± 0.00	0.235 ± 0.011
9.80 ± 0.47	3.04 ± 0.15
17.06 ± 0.12	4.64 ± 0.21
7.71 ± 0.45	2.274 ± 0.067
12.720 ± 0.080	3.76 ± 0.19

$$k = (2.708 \pm 0.061) \times 10^{-11} \text{ cm}^3 \text{ molecule}^{-1} \text{ s}^{-1}.$$

Figure A.13: HBr in N₂, 475 ± 1 K.

[HBr] 10 ¹⁶ molec cm ⁻³	λ μs ⁻¹
0.00 ± 0.00	0.397 ± 0.012
17.88 ± 0.90	6.12 ± 0.39
11.05 ± 0.55	3.57 ± 0.18
15.09 ± 0.76	5.04 ± 0.28
4.14 ± 0.21	1.682 ± 0.065

$$k = (3.054 \pm 0.107) \times 10^{-11} \text{ cm}^3 \text{ molecule}^{-1} \text{ s}^{-1}.$$